World Electric Vehicle Journal

MDPI

Article

Prototype Validation of Accelerated Gradient-Descent-Based Observer and Model-Free Control for a Fuel Cell–Supercapacitor–Battery Hybrid Power Source for e-Vehicle Applications

Orathai Lueyos [1], Pongsiri Mungporn [2,3], Burin Yodwong [3,4], Serge Pierfederici [5], Nicu Bizon [6,7], Anusorn Yodjaiphet [8], Wichet Thipprasert [8], Babak Nahid-Mobarakeh [9] and Phatiphat Thounthong [3,4,10,*]

1 Department of Electrical Engineering, Rajamangala University of Technology Lanna (RMUTL), Chiang Mai 50300, Thailand; orathai_lu66@live.rmutl.ac.th
2 Thai French Innovation Institute, King Mongkut's University of Technology North Bangkok, Bangkok 10800, Thailand; pongsiri.m@tfii.kmutnb.ac.th
3 Renewable Energy Research Centre (RERC), King Mongkut's University of Technology North Bangkok, Bangkok 10800, Thailand; burin.y@fte.kmutnb.ac.th
4 Department of Teacher Training in Electrical Engineering, Faculty of Technical Education, King Mongkut's University of Technology North Bangkok, Bangkok 10800, Thailand
5 Laboratoire d'Energetique et de Mecanique Théorique et Appliquée (LEMTA), UMR, University of Lorraine, 54500 Vandœuvre-lès-Nancy, France; serge.pierfederici@univ-lorraine.fr
6 Pitești University Centre, The National University of Science and Technology POLITEHNICA Bucharest, 110040 Pitesti, Romania; nicu.bizon1402@upb.ro
7 Energy Department, National Research and Development Institute for Cryogenic and Isotopic Technologies, Uzinei Street No. 4, 240050 Ramnicu Valcea, Romania
8 Department of Electrical Engineering, Rajamangala University of Technology Lanna (RMUTL), Chiang Rai 57120, Thailand; wichet_thip@rmutl.ac.th (W.T.)
9 Department of Electrical and Computer Engineering, McMaster University, Hamilton, ON L8S 4L8, Canada; nahidmb@mcmaster.ca
10 Groupe de Recherche en Énergie Électrique de Nancy (GREEN), University of Lorraine, 54500 Nancy, France
* Correspondence: phatiphat.t@fte.kmutnb.ac.th; Tel.: +66-81-917-4058

Abstract

This paper presents the prototype validation of an accelerated gradient observer (AGO)-assisted continuous predictive control (CPC)-based model-free control framework for a fuel-cell/supercapacitor/battery (FC/SC/battery) hybrid power source in electric-vehicle applications. The AGO, based on second-order gradient-descent dynamics, estimates lumped nonlinearities, parameter variations, unmodeled dynamics, and disturbances through ultra-local models. These estimates are integrated into three outer energy-management loops and three inner current-control loops to regulate the DC bus and coordinate multi-time-scale power sharing among the fast supercapacitor, intermediate battery, and slow fuel cell while respecting source constraints. Lyapunov analyses establish nominal tracking convergence and AGO stability under stated assumptions. Simulation comparisons with an extended-state observer (ESO), sliding-mode observer (SMO), and high-order disturbance observer (HODO) show that the AGO provides smooth, overshoot-free estimation under noise-free conditions, although the ESO yields lower ITSE and IAE values. Under measurement noise, the AGO reduces normalized RMSE, error standard deviation, and maximum absolute error by 80%, 95%, and 79%, respectively, relative to the ESO. Experimental tests on a 25 kHz prototype using a real 2.5 kW PEMFC in motoring mode and an FC emulator during regenerative braking confirm stable 96 V DC-bus

Academic Editor: Joeri Van Mierlo

Received: 8 October 2026
Revised: 1 November 2026
Accepted: 23 November 2026
Published: 27 November 2026

Copyright: © 2026 by the authors. Published by MDPI on behalf of the World Electric Vehicle Association. Licensee MDPI, Basel, Switzerland. This article is an open access article distributed under the terms and conditions of the Creative Commons Attribution (CC BY) license.

regulation, approximately 1.6 ms recovery in the SC-only CPL test, coordinated power sharing, energy recovery, and source protection.

Keywords: electric vehicles; gradient-descent; hydrogen fuel cell; supercapacitor; battery; model-free control; continuous predictive control; accelerated gradient observer

1. Introduction

Hydrogen-fed proton-exchange membrane fuel-cell (PEMFC) systems are attractive for electric-vehicle applications because they offer high specific energy, high conversion efficiency, low local emissions, and suitability for long-range and heavy-duty transportation [1,2]. However, vehicle traction power varies rapidly during acceleration, deceleration, hill climbing, and regenerative braking [3]. Because the electrochemical, thermal, and reactant-supply dynamics of a PEMFC are relatively slow, forcing the stack to follow abrupt power changes can cause large voltage drops, reactant starvation, efficiency loss, and accelerated degradation [3,4]. Moreover, in a conventional unidirectional configuration, the PEMFC cannot absorb the regenerative power generated during braking, although recovering this energy can improve vehicle efficiency and driving range [5,6]. Efficient power conversion and energy management are therefore required to regulate the DC bus, meet the changing traction demand, limit rapid PEMFC power variations, and recover braking energy [6]. These requirements motivate the integration of the PEMFC with complementary energy storage devices.

As shown in Figure 1, the hybrid power source considered in this study combines a proton-exchange membrane fuel-cell (PEMFC) stack, hereafter referred to as the FC, with a supercapacitor (SC) bank and a battery bank. The three sources are interfaced through dedicated power converters to a common high-voltage DC bus, which supplies the electric traction motor through a DC–AC inverter [6,7]. The high-voltage DC bus enables the electric traction system to deliver high power while limiting the required current level. The three sources have complementary energy and power characteristics. The FC/hydrogen subsystem provides high specific energy and is therefore suitable for supplying the slowly varying average traction power rather than rapid load transients [8,9]. The battery provides medium-term energy and power support; however, repeated high-current charge - discharge cycles can increase electrical and thermal stresses and accelerate battery degradation [7,8]. In contrast, the SC offers high specific power, rapid bidirectional power capability, and a long cycle life, making it suitable for supplying short acceleration peaks and absorbing regenerative-braking energy. Nevertheless, its low specific energy limits the duration of this support [9,10].

Figure 2 illustrates the need for fast DC-bus voltage regulation by comparing the responses of the hybrid source under different control dynamics through a MATLAB (2026)-based simulation of a load-power step from 5 to 20 kW. Under slow control dynamics, the transient power imbalance persists, producing a DC-bus voltage deviation of approximately 14 V and a settling time of approximately 40 ms. Under fast control dynamics, the SC responds promptly to the load change, reducing the voltage deviation to approximately 12 V and the settling time to approximately 8 ms, while the battery and FC respond over progressively longer time scales. These results demonstrate that stable EV operation requires coordinated multi-time-scale control, in which the SC handles rapid power transients, the battery provides intermediate support, and the FC supplies the slowly varying average power. Such coordination is essential for limiting DC-bus voltage deviations during abrupt traction-power changes [11].

Conventional control strategies for hybrid power sources, including cascaded proportional–integral (PI), [11], sliding-mode control (SMC), [12], Hamiltonian Control, [13], passivity-based control (PBC), [14], and model predictive control (MPC), [15], are generally designed using nominal converter and source dynamics or prescribed uncertainty bounds. Although these model-based approaches can provide systematic closed-loop dynamics, their performance depends strongly on model accuracy and controller tuning.

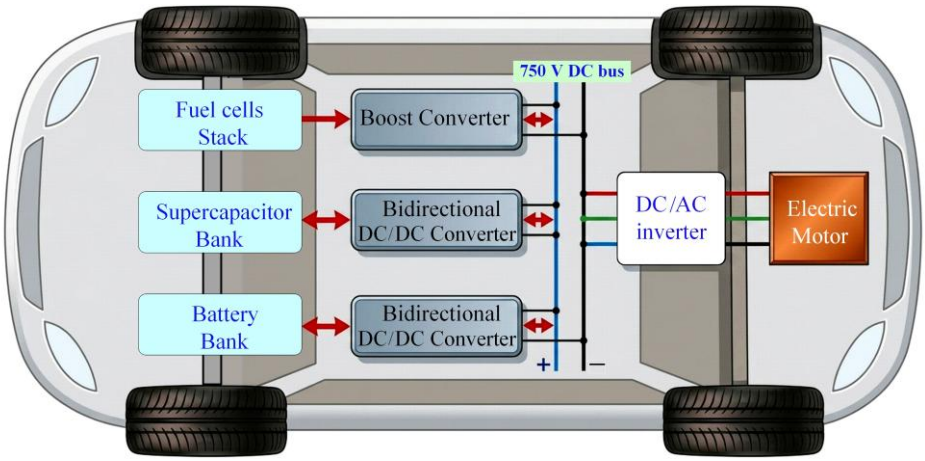


Figure 1. Configuration of the FC/SC/battery hybrid power source connected to a common 750 V DC bus and supplying an electric traction drive through a DC–AC inverter.

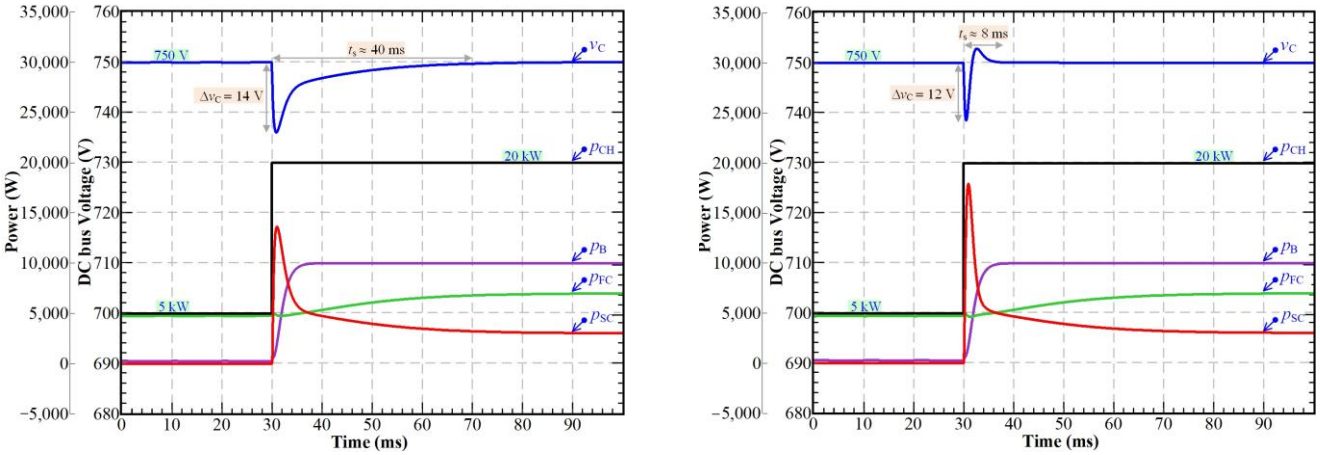


Figure 2. Control motivation for the FC/SC/battery hybrid power source in an electric-vehicle DC microgrid: MATLAB-based comparison of the DC-bus voltage and source-power responses to a load-power step from 5 to 20 kW under (**a**) slow and (**b**) fast control dynamics.

In practice, parameter tolerances, parasitic losses, temperature changes, source-voltage variations, component aging, changing loads, and measurement noise cause the plant dynamics to vary continuously. Model-free control (MFC) reduces this dependence by grouping unknown nonlinearities, parameter variations, unmodeled dynamics, and external disturbances into a lumped term that is estimated online [16,17]. Thus, MFC does not eliminate the need for estimation; instead, it avoids requiring a complete and fixed parametric model. An extended-state observer (ESO) offers a relatively simple structure and adjustable convergence bandwidth, but a high bandwidth may produce peaking or overshoot and amplify measurement noise [18,19]. A sliding-mode observer (SMO) can provide fast finite-time convergence and strong robustness, although its switching mechanism may introduce chattering and noise-sensitive estimates [20]. A high-order

disturbance observer (HODO) can improve the estimation of time-varying disturbances, but its additional states and gains increase tuning difficulty and computational burden [21]. Gradient-descent (GD) learning provides another low-complexity mechanism for updating unknown quantities directly from the tracking error, although its learning rate determines the compromise among convergence speed, oscillation, and noise sensitivity [22,23].

These considerations motivate the gradient-descent-based estimation mechanism developed in this study for fast and smooth lumped-dynamics estimation in MFC. The main contributions of this study are summarized as follows:

(1) Novel Continuous Predictive Control (CPC) Law: A new CPC algorithm is proposed for model-free control based on finite-horizon tracking-error optimization. Unlike conventional model-free control approaches in which the feedback gain is commonly selected through manual tuning, the proposed CPC law analytically determines the control gain from the prediction horizon and sampling period. This formulation provides a systematic tuning mechanism and generates a continuous-valued control command without iterative online optimization.

(2) Novel Accelerated Gradient Observer (AGO): A new AGO algorithm is developed for online estimation of unknown lumped dynamics, including system nonlinearities, parameter uncertainties, and external disturbances. The observer combines integral-augmented state-error correction with gradient-based lumped-dynamics adaptation. Its mathematical formulation provides a systematic basis for observer-gain selection, while comparative simulations against ESO, SMO, and HODO demonstrate improved estimation accuracy under the investigated measurement-noise conditions.

(3) Real-Time Prototype Validation: The proposed CPC and AGO algorithms are integrated into a hierarchical energy-management framework comprising three outer energy-control loops and three inner current-control loops for an FC/SC/battery hybrid power source. The framework requires only four online lumped-dynamics estimates, with two additional energy-side terms reconstructed algebraically. Experimental validation using a dSPACE-based prototype operating at a switching frequency of 25 kHz demonstrates DC-bus regulation, coordinated power sharing, and regenerative-energy recovery.

The remainder of this paper is organized as follows. Section 2 presents the FC/SC/battery hybrid-source configuration, system dynamics, and energy-management objectives. Section 3 develops the proposed AGO-assisted CPC-based framework, including the controller and observer designs, stability analysis, and practical implementation constraints. Section 4 describes the simulation and experimental setups and discusses the comparative and experimental results. Finally, Section 5 presents the conclusions of this study.

2. Hybrid-Source Architecture and Energy-Management Problem Formulation

Figure 3 illustrates the studied FC/SC/battery hybrid power source connected to a common DC bus. The proton-exchange-membrane fuel cell (PEMFC) is interfaced with the DC bus through a unidirectional boost converter, whereas the SC and battery are connected through bidirectional DC–DC converters. Under the adopted average model, the converter–inductor currents are equal to their corresponding source currents:

$$i_{FC} = i_{L1},\ \ i_{SC} = i_{L2},\ \ i_B = i_{L3}. \tag{1}$$

The corresponding FC, SC, and battery powers are defined as

$$p_{FC} = v_{FC} i_{FC},\ p_{SC} = v_{SC} i_{SC},\ p_B = v_B i_B. \tag{2}$$

Under the adopted sign convention, positive source power indicates power delivered to the DC bus. Therefore, $p_{SC} < 0$ and $p_B < 0$ represent SC and battery charging, respectively. Because the FC is connected through a unidirectional converter, its power satisfies $p_{FC} \geq 0$. On the load side, $p_{CH} > 0$ represents motoring, whereas $p_{CH} < 0$ represents regenerative energy returned to the DC bus. Neglecting converter losses only for the supervisory energy-management formulation, the instantaneous power balance is expressed as

$$p_{FC}(t) + p_{SC}(t) + p_B(t) = p_{CH}(t). \quad (3)$$

Equation (3) defines the fundamental power-allocation requirement of the energy-management system. Within this framework, the SC compensates for rapid power variations, the battery maintains the medium-term energy balance, and the FC supplies the slowly varying average power demand. Converter losses, parameter uncertainties, parasitic effects, source nonlinearities, and external disturbances are not assumed to be zero in the implemented controller. Instead, their combined effects are incorporated into the estimated lumped terms of the ultra-local models.

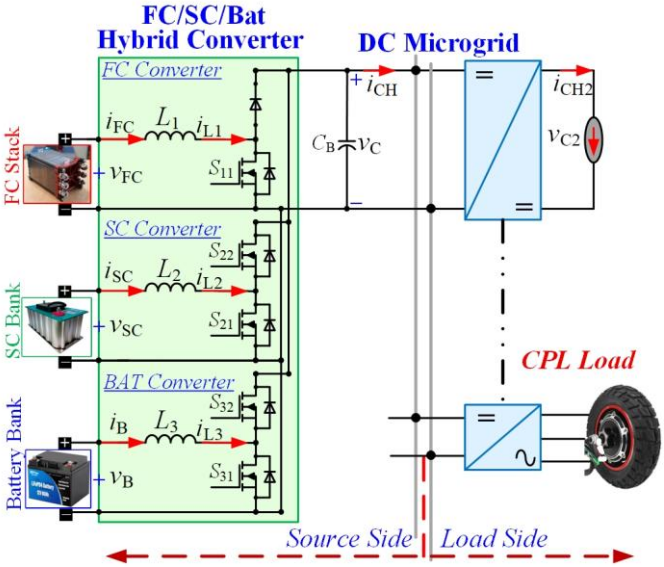


Figure 3. Configuration of the FC/SC/battery hybrid power source connected to a common DC bus and supplying representative traction drive and auxiliary load.

2.1. Fuel-Cell Dynamic Limitation and Fuel-Starvation Risk

A PEMFC generally produces a low and unidirectional DC voltage; therefore, a unidirectional boost converter is employed to connect the FC stack to the higher-voltage DC bus. The converter should operate in continuous-conduction mode to reduce the peak inductor current and FC-current ripple. Excessive ripple and abrupt current variations can impose electrical and mechanical stress on the FC stack and accelerate its degradation [24]. experimentally demonstrated that a rapid load disturbance applied through the converter can produce a sharp FC-current transition that may be harmful to the stack [25].

The dynamic limitation of the FC system is illustrated in Figure 4. When the load changes abruptly from a low to a high level, the converter rapidly increases the FC current to satisfy the power demand. The electrochemical consumption of hydrogen and oxygen therefore increases almost instantaneously. However, the reactant-supply system including the hydrogen valve, air compressor, gas manifolds, pressure regulators, and humidification system responds more slowly because of its mechanical and pneumatic dynamics.

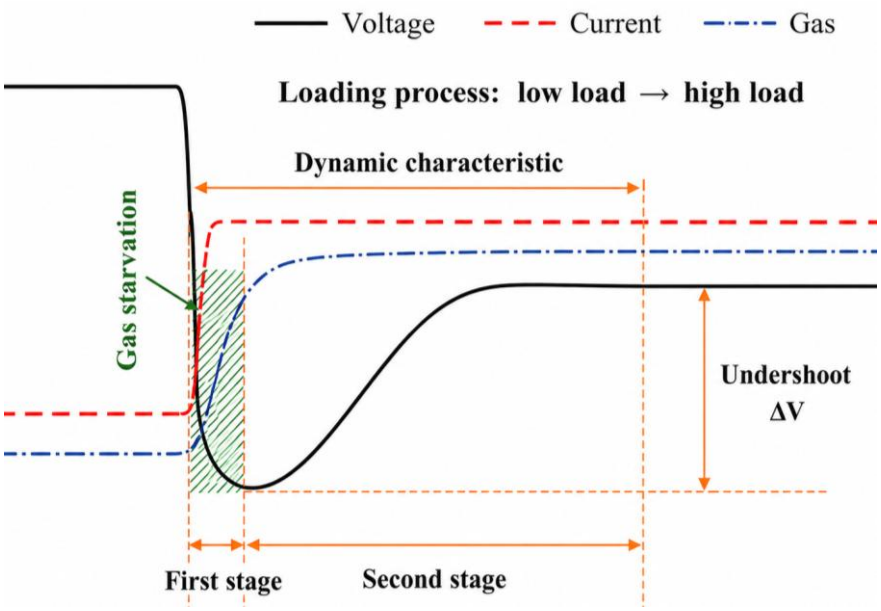


Figure 4. Conceptual transient response of the PEMFC during a low-to-high load transition, showing the FC voltage, FC current, and reactant-flow dynamics, together with the temporary reactant-starvation interval, two-stage voltage response, and voltage undershoot ΔV.

Consequently, a temporary mismatch occurs between the reactant consumption and supply rates, as represented by the shaded reactant-starvation interval in Figure 4.

During the first stage of the transient response, the rapid increase in FC current is accompanied by a sharp voltage reduction because the reactant flow has not yet reached the required level. This supply–demand imbalance can cause hydrogen starvation at the anode or oxygen starvation at the cathode. During the second stage, the reactant flow gradually increases, and the FC voltage recovers toward its new steady state value. The difference between the minimum transient voltage and the final steady-state voltage is defined as the voltage undershoot, ΔV. The magnitude and duration of this undershoot reflect the dynamic reactant-transport limitation of the FC system [26].

Severe or repeated reactant starvation may produce excessive concentration losses, local cell-voltage reversal, carbon-support corrosion, catalyst degradation, and irreversible stack damage. experimentally showed that FC current must be limited and varied gradually to maintain coordination between the reactant-flow rate and the electrochemical current. Recent investigations have similarly emphasized the importance of FC power-rate constraints, gas-feeding control, and oxygen-excess-ratio regulation under dynamic loading conditions [3].

In addition to reactant-supply dynamics, internal water management and mass-transfer limitations significantly influence PEMFC voltage stability under transient operating conditions. Excessive liquid-water accumulation in the gas diffusion layers and flow channels can restrict oxygen transport to the catalyst sites, increasing concentration losses and causing voltage fluctuations. Conversely, insufficient membrane hydration reduces proton conductivity, increases ohmic resistance, and contributes to voltage degradation. These phenomena have been extensively investigated in the PEMFC literature [27]. Accordingly, the proposed energy-management strategy limits rapid FC power and current variations to reduce abrupt reactant demand, while the SC and battery compensate for fast load transients. However, direct regulation of membrane hydration, liquid-water distribution, and reactant-supply dynamics is beyond the scope of the present study.

Accordingly, the magnitude and rate of change of the FC current reference should be constrained as

$$0 \le i_{FC}^{*} \le i_{FC,max}, \left|\frac{di_{FC}^{*}}{dt}\right| \le r_{FC,max}, \quad (4)$$

where $i_{FC,max}$ denotes the maximum allowable FC current and $r_{FC,max}$ represents its maximum allowable rate of change. Therefore, the FC is assigned to supply the slowly varying average power, whereas the SC rapidly compensates for the transient power difference. The battery supports medium-term energy balancing. This complementary power-sharing strategy prevents abrupt FC-current variations, reduces the voltage undershot, and mitigates the risks of reactant starvation and premature FC degradation. If the available FC power decreases because of fuel starvation, the battery and SC may temporarily compensate for the power deficit within their operating limits. However, DC-bus regulation cannot be guaranteed when the total available source power becomes insufficient. Direct detection of reactant starvation is outside the scope of the present study.

2.2. Dynamic Characteristics of the FC/SC/Battery Hybrid Source

The hybrid source is therefore organized according to three distinct dynamic roles. The SC provides the fastest power response and compensates for abrupt power imbalance at the DC bus. The battery provides intermediate power support and restores the SC energy over a slower time scale. The FC provides the slow average power required by the system and is deliberately prevented from following rapid load variations. This dynamic hierarchy is consistent with the physical energy-management principle previously established for FC/SC/battery hybrid sources.

Figure 5a illustrates the desired power-sharing response to a positive load-power step during motoring operation. At $t = 20$ s, the constant-power-load (CPL) power increases abruptly from zero to approximately 4.5 *pu*. Because the FC and battery cannot respond instantaneously, the SC initially supplies nearly the entire load-power demand. The SC power subsequently decreases as the battery and FC powers gradually increase. The battery reaches its assigned power level more rapidly than the FC, thereby providing medium-term transient support. Meanwhile, the FC power increases slowly toward its prescribed operating point, avoiding an abrupt FC-current variation and the associated fuel-starvation risk. At steady state, the three source powers satisfy the load-power demand, with the FC, battery, and SC supplying approximately 1.0, 1.5, and 2.0 *pu*., respectively.

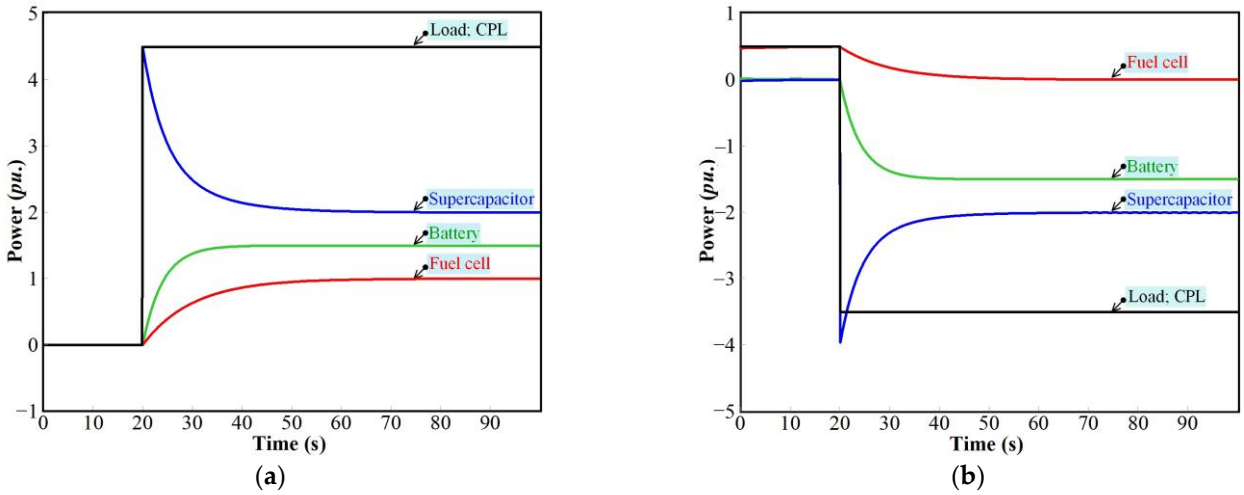


Figure 5. Conceptual power-sharing responses of the FC/SC/battery hybrid source to: (**a**) a positive load-power step during motoring operation; and (**b**) a negative load-power step during regenerative-braking operation.

Figure 5b presents the corresponding response to a negative load-power step representing regenerative braking. Before the transition, the FC supplies approximately 0.5 pu. to meet the initial positive demand. At $t = 20$ s, the load power changes abruptly to approximately -3.5 pu. Because the FC is connected through a unidirectional converter and cannot absorb regenerative power, its command is gradually reduced to zero. Immediately after the transition, the SC absorbs both the regenerative load power and the residual power still supplied by the FC; consequently, its transient power reaches approximately -4.0 pu. The battery then begins to absorb the medium-term regenerative power, causing the SC absorption power to decrease gradually. At steady state, the battery and SC absorb approximately-1.5 and -2.0 pu., respectively, while the FC power remains zero.

To produce these different dynamic responses, the supervisory power commands are limited and then passed through command-shaping filters. The constrained battery-power command $p_{B,C}$ is passed through a second-order filter to generate the desired battery-power command $p_{B,d}$:

$$\frac{p_{B,d}(s)}{p_{B,C}(s)} = \frac{\omega_B^2}{s^2 + 2\zeta_B\omega_B s + \omega_B^2}, \tag{5}$$

where $\omega_B > 0$ and $\zeta_B > 0$ are the natural frequency and damping ratio of the battery command-shaping filter, respectively. The natural frequency determines how rapidly the battery command changes, whereas the damping ratio determines the oscillatory behavior of the response.

Similarly, the constrained FC-power command $p_{FC,C}$ is shaped to generate the desired FC-power command $p_{FC,d}$:

$$\frac{p_{FC,d}(s)}{p_{FC,C}(s)} = \frac{\omega_{FC}^2}{s^2 + 2\zeta_{FC}\omega_{FC} s + \omega_{FC}^2}, \tag{6}$$

where $\omega_{FC} > 0$ and $\zeta_{FC} > 0$ denote the natural frequency and damping ratio of the FC command-shaping filter, respectively. To make the battery respond faster than the FC, the filter frequencies are selected such that $\omega_B > \omega_{FC}$.

Thus, the FC command changes slowly, the battery command changes at a medium rate, and the SC directly compensates for the remaining fast power imbalance. Both filters have unity steady-state gain; therefore, they shape the transient response without changing the final value of the corresponding power command.

The battery supports bidirectional power flow and must satisfy both its power and current limits:

$$p_{B,\min} \le p_{B,d} \le p_{B,\max},\ i_{B,\min} \le i_{B,d} \le i_{B,\max}. \tag{7}$$

The negative lower limits allow the battery to absorb regenerative power, whereas the positive upper limits restrict the power delivered during motoring operation. Because the FC converter is unidirectional, the FC can only supply positive power. Its desired power and current commands must therefore satisfy.

$$0 \le p_{FC,d} \le p_{FC,\max},\ 0 \le i_{FC,d} \le i_{FC,\max}. \tag{8}$$

Applying both power and current limits provides two levels of protection for the FC and battery. The power limits prevent the supervisory controller from requesting power outside the permissible operating range. The current limits prevent excessive source currents, particularly when the FC or battery voltage varies. Consequently, the proposed command-shaping and limiting process produces complementary responses illustrated in Figure 5.

3. Proposed AGO-Assisted CPC-Based MFC Framework

3.1. Ultra-Local Model

Consider a general single-input single-output nonlinear system. Over a sufficiently short time interval, its unknown dynamics can be represented by the following first-order ultra-local model [16,28,29]:

$$\dot{x}(t) = F(t) + \alpha u(t), \tag{9}$$

where $x(t)$ is the measured controlled variable, $u(t)$ is the physical control input, and $\alpha \neq 0$ is a designer-selected scaling coefficient. The value of α is selected so that $\alpha u(t)$ and $\dot{x}(t)$ have comparable magnitudes. The lumped term $F(t)$ represents all unknown or incompletely known system behavior, including the nonlinear plant dynamics, parameter uncertainties, parameter effects, parasitic effects, coupling terms, and external disturbances.

The main advantage of the ultra-local model in (9) is that the controller does not require a complete analytical model of the physical system. Instead, all unknown and uncertain dynamics are combined into the single lumped term $F(t)$. The proposed AGO, estimates this lumped term online using the available measured signals and continuously provides the estimate $\hat{F}(t)$ to the controller.

Substituting this ideal law into (10) yields

$$\dot{x}(t) = \lambda(t). \tag{10}$$

This equation illustrates the core principle of the proposed CPC framework presented in Appendix A.1. Once the unknown dynamics are compensated for, the system trajectory can be directly shaped through $\lambda(t)$ to achieve the desired tracking-error convergence and transient response using continuous predictive control.

For a desired trajectory $x_d(t)$ the tracking error is defined as

$$e(t) = x(t) - x_d(t) \tag{11}$$

The MFC objective is to determine $u(t)$ such that $e(t) \to 0$ without requiring an explicit analytical expression for $F(t)$. Because $F(t)$ is unknown in practice [30,31], the real-time estimate $\hat{F}(t)$ generated by the AGO is used instead, yielding the following implementable MFC law:

$$u(t) = \frac{\lambda(t) - \hat{F}(t)}{\alpha}. \tag{12}$$

Figure 6 illustrates the interaction between the AGO and the CPC-based MFC law. The controller uses the reference $x_d(t)$, the measured output $x(t)$, and the estimated lumped dynamics $\hat{F}(t)$, generated by the AGO to calculate the control input required to impose the desired dynamics $\lambda(t)$. The observer uses the measured state $x(t)$ and the applied control input $u(t)$ to estimate both $\hat{x}$ and $\hat{F}$. As the observer converges such that

$$\hat{x}(t) \to x(t), \quad \hat{F}(t) \to F(t), \tag{13}$$

the estimation errors vanish, and the closed-loop system approaches the desired behavior prescribed by the CPC law.

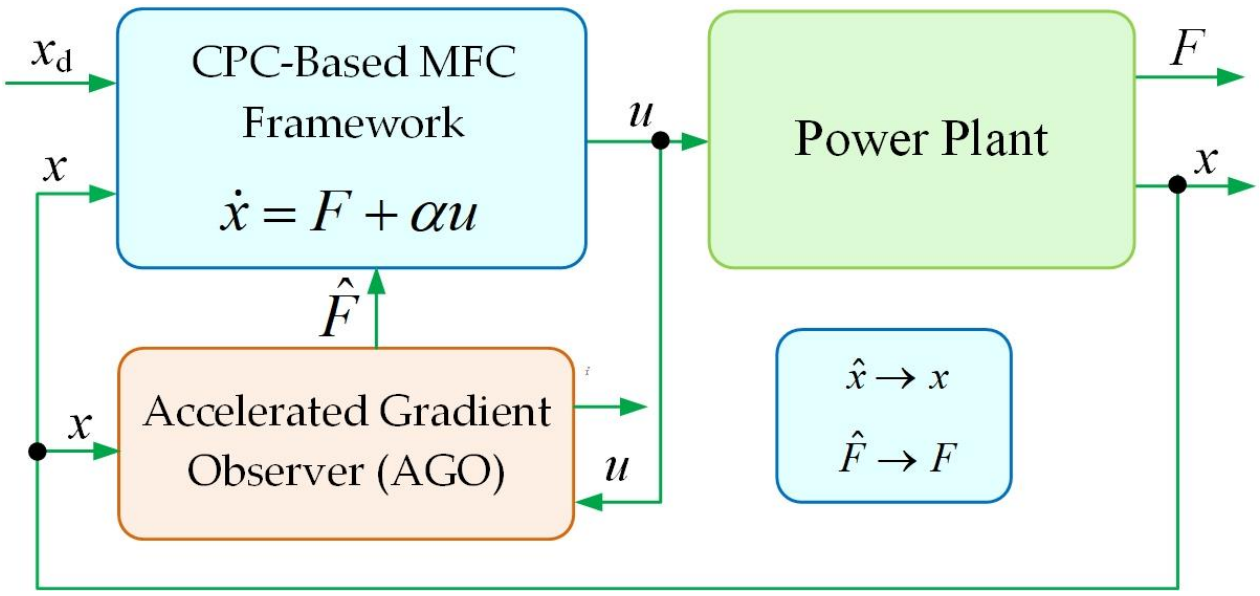


Figure 6. Proposed AGO-assisted CPC-based MFC structure for online lumped-dynamics estimation and control of the hybrid power-source converters.

3.2. AGO-Assisted CPC-Based MFC Formulation

The CPC law generates the desired state derivative as

$$\lambda_{CPC} = -K_{CPC} e, \qquad K_{CPC} = \frac{3}{(2N+1)T_s}, \tag{14}$$

where N is the prediction horizon and T_s is the sampling period. The corresponding AGO-assisted model-free control law is expressed as

$$u = \text{sat}\left(\frac{\lambda_{CPC} - \hat{F}}{\alpha}, u_{min}, u_{max}\right). \tag{15}$$

The complete finite-horizon derivation of the CPC gain and the corresponding stability analysis are provided in Appendix A. The AGO estimates the lumped dynamics F without requiring an explicit physical model.

The state-estimation error is defined as

$$e_x = x - \hat{x}, \tag{16}$$

For the ultra-local model in (9), the AGO is formulated as

$$e_o = \eta_x e_x + \eta_a a_x, \tag{17}$$

$$\dot{a_x} = e_x, \tag{18}$$

$$\dot{\hat{x}} = \hat{F} + \alpha u + e_o, \tag{19}$$

$$\dot{\hat{F}} = \eta_F \frac{e_o}{\omega_o}. \tag{20}$$

Here, a_x is an auxiliary integral state, e_o is the composite observer-error signal, and η_x, η_a and η_F are positive observer gains. The state-estimation dynamics are governed by η_x and η_a whereas η_F determines the adaptation rate of the lumped-dynamics estimate.

The proposed CPC and AGO algorithms address two complementary problems in model-free control. The CPC law determines the desired closed-loop dynamics through analytical finite-horizon optimization, whereas the AGO reconstructs the unknown

lumped dynamics required for their realization. Unlike conventional proportional-only observer correction, the proposed AGO introduces an auxiliary integral state and a gradient-based reconstruction law driven by the composite estimation-error signal. The resulting structure allows the controller and observer to be designed systematically without requiring a complete parametric model of the physical system.

3.3. Modeling and Control Requirements of the FC/SC/Battery Hybrid Power Source

3.3.1. Physical Model of the FC/SC/Battery Hybrid Power Source

Using the conventional averaged converter representation [32], the FC-current dynamics, the SC-current dynamics and the battery-current dynamics can be expressed as follows [33]

$$\frac{di_{FC}}{dt}=\frac{v_{FC}-r_{L1}i_{FC}-v_C+d_1v_C}{L_1}, \tag{21}$$

$$\frac{di_{SC}}{dt}=\frac{v_{SC}-r_{L2}i_{SC}-v_C+d_2v_C}{L_2}, \tag{22}$$

$$\frac{di_B}{dt}=\frac{v_B-r_{L3}i_B-v_C+d_3v_C}{L_3}, \tag{23}$$

The DC-bus voltage dynamics are

$$C_B\frac{dv_C}{dt}=(1-d_1)i_{FC}+(1-d_2)i_{SC}+(1-d_3)i_B-i_{CH}-\frac{v_C}{r_p}, \tag{24}$$

where C_B is the DC-bus capacitance, r_p represents the equivalent parallel loss resistance, and i_{CH} is the current exchanged with the load-side converter.

$$E_C=\frac{1}{2}C_Bv_C^2,\quad E_{SC}=\frac{1}{2}C_{SC}v_{SC}^2,\quad E_B(t)=E_{B,\,ini}-\int_0^t v_B(\tau)i_B(\tau)d\tau. \tag{25}$$

Because positive battery current denotes discharge, the battery energy decreases when p_B is positive. The battery SOC is estimated from [34]

$$SOC(t)=100\frac{E_B(t)}{E_{B,\,max}},\quad E_{B,\,max}=3600v_{B,\,nom}Q_B, \tag{26}$$

where Q_B is expressed in ampere-hours. The energy dynamics are

$$\frac{dE_C}{dt}=p_{FC}+p_{SC}+p_B-p_{CH}-\frac{v_C^2}{r_p},\quad \frac{dE_{SC}}{dt}=-p_{SC},\quad \frac{dE_B}{dt}=-p_B. \tag{27}$$

Two composite energy variables are introduced to establish hierarchical coordination among the energy sources:

$$E_{T1}=E_C+E_{SC},\quad E_{T2}=E_C+E_{SC}+E_B. \tag{28}$$

Their dynamics are obtained as

$$\frac{dE_{T1}}{dt}=p_{FC}+p_B-p_{CH}-\frac{v_C^2}{r_p},\quad \frac{dE_{T2}}{dt}=p_{FC}-p_{CH}-\frac{v_C^2}{r_p},\qquad \alpha_{E1}=\alpha_{E2}=\alpha_{E3}=1. \tag{29}$$

The three current channels are expressed in the ultra-local form

$$\frac{di_{Lj}}{dt}=F_{Ij}+\alpha_{Ij}d_j,\quad \alpha_{Ij}=\frac{v_C}{L_j},\quad j\in\{1,2,3\}, \tag{30}$$

where j = 1, 2, and 3 correspond to the FC, SC, and battery branches, respectively. The terms F_{I1}, F_{I2}, and F_{I3} contain the unknown source voltages, converter losses, parasitic resistances, parameter variations, and other unmodeled current-channel dynamics.

Similarly, the three outer energy channels are written as

$$\frac{dE_C}{dt}=F_{E1}+p_{SC},\quad \frac{dE_{T1}}{dt}=F_{E2}+p_B,\quad \frac{dE_{T2}}{dt}=F_{E3}+p_{FC}. \tag{31}$$

Only F_{E1} is directly learned by the AGO. The other two energy-side lumped terms are reconstructed algebraically as

$$\hat{F}_{E2}=\hat{F}_{E1}-p_B,\quad \hat{F}_{E3}=\hat{F}_{E1}-p_{FC}-p_B. \tag{32}$$

Consequently, only four lumped terms are estimated online:

$$\hat{F}_{I1},\ \hat{F}_{I2},\ \hat{F}_{I3},\ \hat{F}_{E1}. \tag{33}$$

This configuration avoids two additional energy observers while providing all six lumped terms required by the three outer energy loops and three inner current loops.

3.3.2. Control Objectives

Co_I. regulates v_C through $E_C \rightarrow E_{C,d}$.

Co_II. restores the SC energy through $E_{T1} \rightarrow E_{T1,d}$.

Co_III. maintains the battery SOC through $E_{T2} \rightarrow E_{T2,d}$, with $SOC_d = 80\%$ in the experimental tests.

Co_IV. imposes the dynamic hierarchy; SC: fastest > battery; Intermediate > FC: slowest.

Co_V. prevents rapid FC power variations and reverse FC power flow.

Co_VI. ensures that the SC operates within its allowable voltage and current limits,

$$v_{SC,min} \le v_{SC} \le v_{SC,max},\ i_{SC,min} \le i_{SC} \le i_{SC,max}$$

Co_VII. satisfies battery power and current constraints,

$$p_{B,min} \le p_{B,d} \le p_{B,max},\ i_{B,min} \le i_{B,d} \le i_{B,max}$$

Co_VIII. satisfies FC power/current constraints,

$$0 \le p_{FC,d} \le p_{FC,max},\ 0 \le i_{FC,d} \le i_{FC,max}$$

3.3.3. Outer Energy Management, Sources Protection, and Inner Current Control

The desired DC-bus, SC, battery, and composite energy are defined as

$$E_{C,d}=\frac{1}{2}C_B v_{C,d}^2,\quad E_{SC,d}=\frac{1}{2}C_{SC}v_{SC,d}^2,\quad E_{B,d}=\frac{SOC_d}{100}E_{B,max}, \tag{34}$$

$$E_{T1,d}=E_{C,d}+E_{SC,d},\quad E_{T2,d}=E_{C,d}+E_{SC,d}+E_{B,d}. \tag{35}$$

To satisfy Co_III, the desired battery SOC is set to ($SOC_d = 80\%$) for the experimental tests. The three outer-loop energy errors are defined as

$$e_{E1}=E_C-E_{C,d},\quad e_{E2}=E_{T1}-E_{T1,d},\quad e_{E3}=E_{T2}-E_{T2,d}. \tag{36}$$

For $n \in \{1,2,3\}$, CPC generates the desired energy dynamics as

$$\lambda_{En}=-K_{En}e_{En},\quad K_{En}=\frac{3}{(2N_{En}+1)T_s}. \tag{37}$$

The three raw source-power commands are therefore

$$p^{*}_{SC,\,d} = \lambda_{E1} - \hat{F}_{E1}, \quad p^{*}_{B,\,d} = \lambda_{E2} - \hat{F}_{E2}, \quad p^{*}_{FC,\,d} = \lambda_{E3} - \hat{F}_{E3}. \tag{38}$$

The first relation in (37) implements Co_I and forms the fastest DC-bus energy-control channel by generating the SC-power command. The second relation implements Co_II by restoring the SC energy through the battery, whereas the third relation implements Co_III by restoring the battery energy through the FC. Together, the three relations, their respective control gains, and the command-shaping dynamics of the battery and FC enforce Co_IV.

These three energy-to-power-to-current-reference relations can be summarized as

$$E_{Cd} \rightarrow p_{SC,\,d} \rightarrow i_{SC,\,d} \rightarrow d_2,$$

$$E_{T1d} \rightarrow p_{B,\,d} \rightarrow i_{B,\,d} \rightarrow d_3,$$

$$E_{T2d} \rightarrow p_{FC,\,d} \rightarrow i_{FC,\,d} \rightarrow d_1.$$

The desired converter currents are allocated according to

$$i_{L1,\,d} = i_{FC,\,d}, \quad i_{L2,\,d} = i_{SC,\,d}, \quad i_{L3,\,d} = i_{B,\,d}. \tag{39}$$

For $j \in \{1,2,3\}$, the current-tracking error and desired CPC dynamics are

$$e_{I,\,j} = i_{L,\,j} - i_{Lj,\,d}, \quad \lambda_{I,\,j} = -K_{I,\,j} e_{I,\,j}, \quad K_{I,\,j} = \frac{3}{(2N_{I,\,j} + 1)T_s}. \tag{40}$$

Using the AGO estimates of the current-side lumped dynamics, the three converter duty ratios are calculated from the unified control law

$$d_j = \mathrm{sat}\left(\frac{\lambda_{I,\,j} - \hat{F}_{Ij}}{\alpha_{I,\,j}}, d_{min}, d_{max}\right), \quad j \in \{1,2,3\}. \tag{41}$$

Thus, the same CPC-MFC structure is applied to all three converter current loops without requiring their complete physical models.

The unconstrained SC-current reference is calculated from the SC-power command as

$$i^{*}_{SC,\,d} = \frac{p_{SC,\,d}}{v_{SC}}, \tag{42}$$

To protect the SC against overdischarge and overcharge, the voltage-dependent SC current limits are defined as

$$i^{P}_{SC,\,max} = \begin{cases} 0, & v_{SC} \le v_{SC,\,min}, \\ i_{SC,\,max}, & v_{SC} > v_{SC,\,min}, \end{cases} \quad i^{P}_{SC,\,min} = \begin{cases} 0, & v_{SC} \ge v_{SC,max}, \\ i_{SC,\,min}, & v_{SC} < v_{SC,max}. \end{cases} \tag{43}$$

The protected SC-current command is then obtained as

$$i_{SC,\,d} = \mathrm{sat}\left(i^{*}_{SC,\,d}, i^{P}_{SC,\,min}, i^{P}_{SC,\,max}\right). \tag{44}$$

Consequently, further SC discharge is inhibited when the SC voltage is at or below its minimum limit, whereas further charging is inhibited when the SC voltage is at or above its maximum limit [35], thereby satisfying Co_VI.

To implement the first protection stage in Co_VII, the raw battery-power command is limited within the allowable power range as

$$p_{B,\,C} = \mathrm{sat}\left(p^{*}_{B,\,d}, p_{B,\,min}, p_{B,\,max}\right). \tag{45}$$

The constrained power command is subsequently passed through the battery command-shaping dynamics defined in (5), producing $p_{B,d}$. The resulting battery-current command is

$$i_{B,d}^{*}=\frac{p_{B,d}}{v_B}, \tag{46}$$

$$i_{B,d}=\mathrm{sat}\left(i_{B,d}^{*}, i_{B,\min}, i_{B,\max}\right). \tag{47}$$

Equations (45) and (46) provide battery protection at both power and current levels. Because the FC converter is unidirectional and cannot absorb regenerative power, the first protection stage in Co_VIII limits the raw FC-power command to nonnegative values as

$$p_{FC,C}=\mathrm{sat}\left(p_{FC,d}^{*}, 0, p_{FC,\max}\right). \tag{48}$$

The constrained FC-power command is passed through the slower FC command-shaping dynamics defined in (6), producing $p_{FC,C}$. The FC-current command is then limited as

$$i_{FC,d}^{*}=\frac{p_{FC,d}}{v_{FC}}, \tag{49}$$

$$i_{FC,d}=\mathrm{sat}\left(i_{FC,d}^{*}, 0, i_{FC,\max}\right). \tag{50}$$

Power saturation prevents reverse FC power flow, while the command-shaping dynamics restrict rapid FC-power variations, thereby satisfying Co_V. The subsequent current saturation prevents excessive FC current when the stack voltage decreases and completes the two-stage protection required by Co_VIII.

3.3.4. AGO Implementation

The four AGO channels are collected into the state, estimated-state, lumped-dynamics, and known-input vectors:

$$\mathbf{x}=\begin{bmatrix} i_{L1} \\ i_{L2} \\ i_{L3} \\ E_C \end{bmatrix}, \quad \hat{\mathbf{F}}=\begin{bmatrix} \hat{F}_{I1} \\ \hat{F}_{I2} \\ \hat{F}_{I3} \\ \hat{F}_{E1} \end{bmatrix}, \quad \boldsymbol{\alpha}=\begin{bmatrix} \alpha_{I1} \\ \alpha_{I2} \\ \alpha_{I3} \\ \alpha_{E1} \end{bmatrix}, \quad \mathbf{u}=\begin{bmatrix} d_1 \\ d_2 \\ d_3 \\ p_{SC} \end{bmatrix}. \tag{51}$$

Accordingly, the four ULM channels are compactly expressed as

$$\dot{\mathbf{x}}=\mathbf{F}+\boldsymbol{\alpha}\odot\mathbf{u}. \tag{52}$$

where $\odot$ denotes elementwise multiplication. Equivalently, this is defined as

$$\mathbf{A}_{\alpha}=\mathrm{diag}\left(\alpha_{I1}, \alpha_{I2}, \alpha_{I3}, \alpha_{E1}\right). \tag{53}$$

Following the AGO formulation developed in Section 3.2, the state-estimation error is defined as

$$\mathbf{e}_x=\mathbf{x}-\hat{\mathbf{x}}. \tag{54}$$

The estimated-state and the AGO correction signal are defined as

$$\frac{d\hat{\mathbf{x}}}{dt}=\hat{\mathbf{F}}+\mathbf{A}_{\alpha}\mathbf{u}+\mathbf{e}_o, \tag{55}$$

$$\mathbf{e}_o=\mathbf{H}_x\mathbf{e}_o+\mathbf{H}_a\dot{\mathbf{a}}, \quad \dot{\mathbf{a}}=\mathbf{e}_x, \tag{56}$$

https://doi.org/10.3390/wevj17120631

$$\frac{d\hat{\mathbf{F}}}{dt} = \mathbf{H}_F \mathbf{H}_a^{-1/2} \mathbf{e}_o. \tag{57}$$

Here, $\mathbf{H}_x$, $\mathbf{H}_a$, and $\mathbf{H}_F$ are positive-definite diagonal learning-rate matrices associated with the state-estimation error, the auxiliary integral state, and the lumped-dynamics estimate, respectively:

$$\mathbf{H}_x = \mathrm{diag}\,(\eta_{x,I1}, \eta_{x,I2}, \eta_{x,I3}, \eta_{x,E1}) \succ 0, \tag{58}$$

$$\mathbf{H}_a = \mathrm{diag}\,(\eta_{a,I1}, \eta_{a,I2}, \eta_{a,I3}, \eta_{a,E1}) \succ 0, \tag{59}$$

$$\mathbf{H}_F = \mathrm{diag}\,(\eta_{F,I1}, \eta_{F,I2}, \eta_{F,I3}, \eta_{F,E1}) \succ 0. \tag{60}$$

Thus, the AGO directly estimates only four lumped-dynamics terms: $\hat{F}_{I1}$, $\hat{F}_{I2}$, $\hat{F}_{I3}$, and $\hat{F}_{E1}$. The complete gain definitions, signal-normalization method, and time-scale-based tuning procedure are provided in Appendix C.3.

3.4. Practical Robustness and Implementation Considerations

The proposed CPC–AGO framework addresses parameter uncertainties, unknown nonlinearities, and external disturbances through the ultra-local model, in which these effects are incorporated into the lumped term F and estimated online by the AGO. Consequently, the controller does not require accurate knowledge of individual physical parameters. However, measurement noise directly affects the observer feedback signals and may influence estimation accuracy. The comparative simulation results in Section 4.2 demonstrate the noise-attenuation capability of the proposed AGO under the investigated conditions. In addition, digital implementation introduces sampling, discretization, and computational-delay effects that are not explicitly considered in the nominal continuous-time stability analysis. The experimental controller operates with a sampling period of 40 μs, demonstrating practical real-time implementation under the tested conditions.

Furthermore, actuator saturation is intentionally incorporated into the control laws in Equations (15) and (41) to restrict the duty ratios to their physically admissible limits, typically $0 \le d \le 1$, or narrower practical operating ranges. These constraints are essential for converter protection and safe operation. Nevertheless, active saturation may temporarily prevent the controller from achieving the desired control action, resulting in tracking deviations. Therefore, the nominal asymptotic stability analysis applies under its stated assumptions, whereas measurement noise, sampling effects, time-varying uncertainties, and actuator saturation may affect practical closed-loop performance. Global asymptotic convergence under arbitrary nonideal conditions is not claimed.

During rapid load variations, the estimation accuracy of the AGO and the tracking performance of the CPC depend on the observer bandwidth, sampling period, measurement noise, and actuator constraints. The experimental results under CPL disturbances demonstrate stable DC-bus regulation using a sampling period of 40 μs. Nevertheless, these results validate the proposed framework under the investigated operating conditions rather than establishing a general stability guarantee under arbitrary disturbances.

3.5. Summary of the Proposed AGO-Assisted CPC-Based MFC Framework

Figure 7 summarizes the proposed AGO-assisted CPC-based MFC framework for the FC/SC/battery hybrid source. The framework comprises an outer energy-management layer, an inner current-control layer, source-protection functions, power-reference filters, an energy-estimation block, and a multichannel AGO.

The outer energy-management layer contains three CPC-based MFC loops. The DC-bus energy loop regulates E_C and generates the desired SC power $p_{SC,d}$, allowing the

SC to compensate for rapid load-power variations. The SC-energy restoration loop regulates E_{T1} and generates the desired battery power $p_{B,d}$, enabling the battery to provide medium-term power support and restore the SC energy. The battery-energy/SOC loop regulates E_{T2} and generates the desired FC power $p_{FC,d}$, allowing the FC to supply the slowly varying average power and maintain the battery SOC near its reference value.

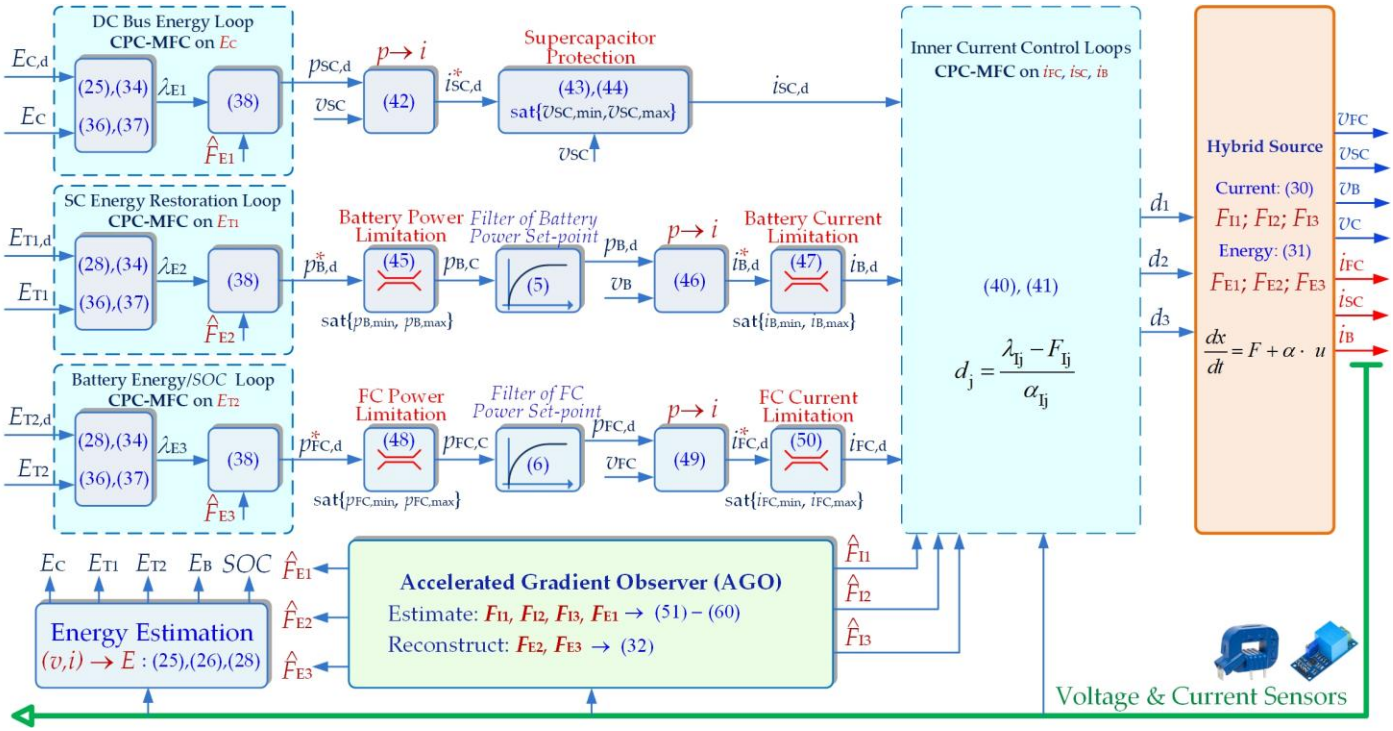


Figure 7. Overall architecture of the proposed AGO-assisted CPC-based MFC framework for the FC/SC/battery hybrid source.

The preliminary battery and FC power references, $p^*_{B,d}$ and $p^*_{FC,d}$, are restricted by their corresponding power limits. The constrained references are subsequently processed by power-reference filters to prevent abrupt variations in battery and FC power. The final power references $p_{SC,d}$, $p_{B,d}$ and $p_{FC,d}$ are then converted into the preliminary current references $i^*_{SC,d}$, $i^*_{B,d}$, and $i^*_{FC,d}$, respectively. The SC voltage-protection function and the battery and FC current-limitation functions ensure that all three sources operate within their allowable voltage and current ranges. The inner CPC-based MFC loops regulate the FC, SC, and battery currents and generate the converter duty ratios d_1, d_2 and d_3. The desired current derivatives generated by the CPC laws are combined with the estimated current-side lumped dynamics $\hat{F}_{I1}$, $\hat{F}_{I2}$, and $\hat{F}_{I3}$. The resulting duty ratios are subsequently applied to the corresponding converters through the PWM units. The measured source voltages and currents are used to calculate the controlled energy variables and are simultaneously supplied to the AGO. The AGO directly provides the lumped dynamics estimates $\hat{F}_{I1}$, $\hat{F}_{I2}$, $\hat{F}_{I3}$ and $\hat{F}_{E1}$. The remaining energy-side estimates, $\hat{F}_{E2}$ and $\hat{F}_{E3}$, are reconstructed and supplied to their corresponding outer energy-control loops.

4. Performance Validations

4.1. Test Bench Description

Figures 7–9 provide an overview of the proposed controller and the experimental platform. Figure 7 presents the overall control architecture. Figure 8 shows the real-time connection of the laboratory equipment. Figure 9 shows the physical experimental

platform. The system includes a 2.5 kW PEMFC stack, a 48 V and 100-Ah Li-ion battery, two SC modules rated at 6 F and 160 V, three power converters, an electronic load, voltage and current sensors, and measurement oscilloscopes. The proposed control algorithm is developed in MATLAB/Simulink and implemented in real time using a dSPACE MicroLabBox. The dSPACE ControlDesk software is used to monitor the system, adjust the control parameters, and record the experimental data. The controller operates with a sampling period of 40 μs and a switching frequency of 25 kHz. The converter parameters are provided in Table 1, while the control parameters and operating limits are summarized in Table 2. Additional information on the experimental equipment, including manufacturers, model numbers, measurement instrumentation, and real-time controller hardware specifications, is provided in Appendix D to facilitate experimental reproducibility.

The term 'prototype' in this study refers to a physical laboratory-scale FC/SC/battery hybrid power-source platform used to validate the proposed CPC and AGO algorithms. The objective of this prototype is to demonstrate the feasibility of the proposed control methodology through simulation and real-time experimental implementation, rather than to reproduce the full power rating of a commercial hydrogen electric vehicle. Therefore, the experimental platform serves as an intermediate validation stage between theoretical algorithm development and potential full-scale vehicle implementation.

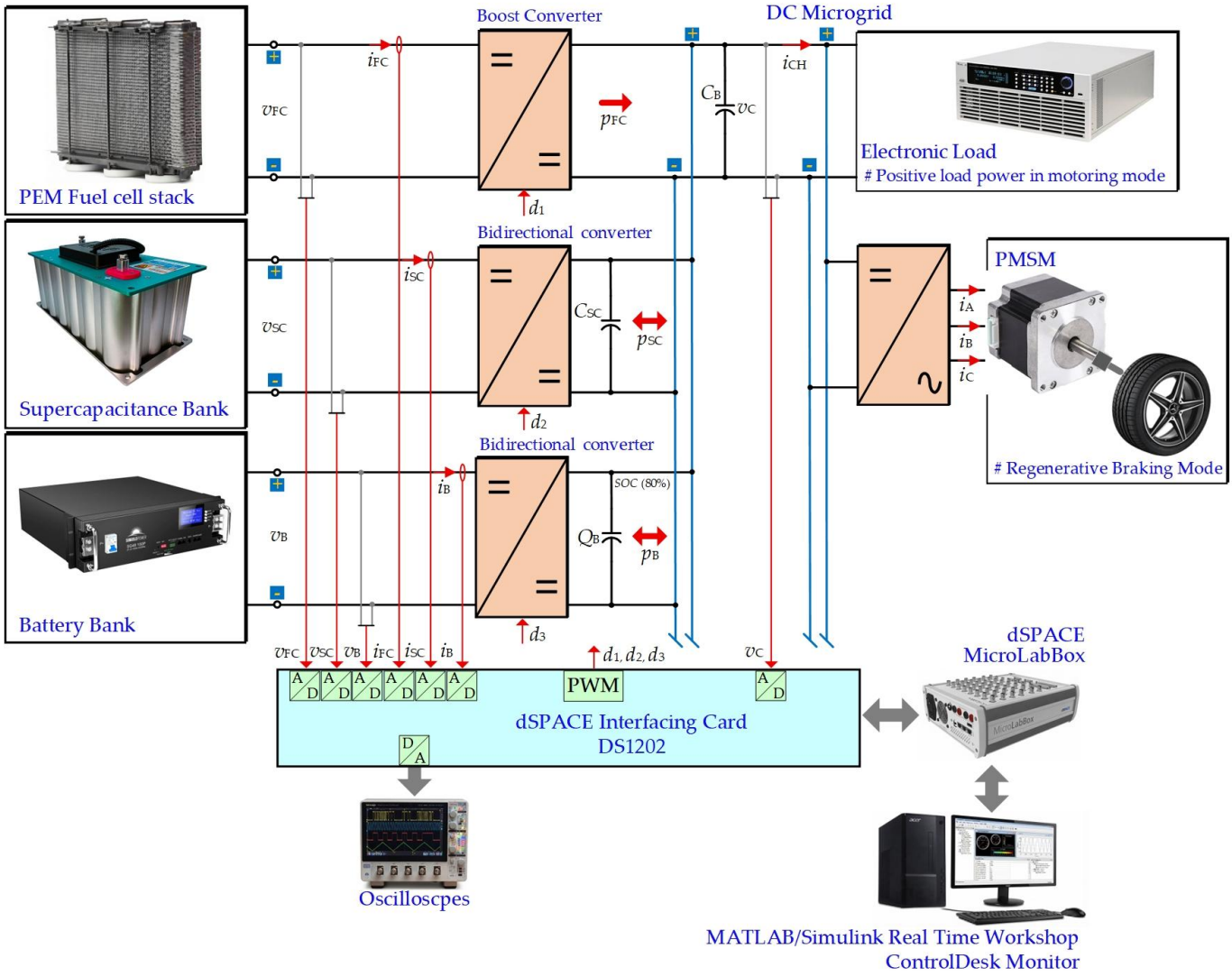


Figure 8. Real-time implementation and electrical configuration of the laboratory test bench.

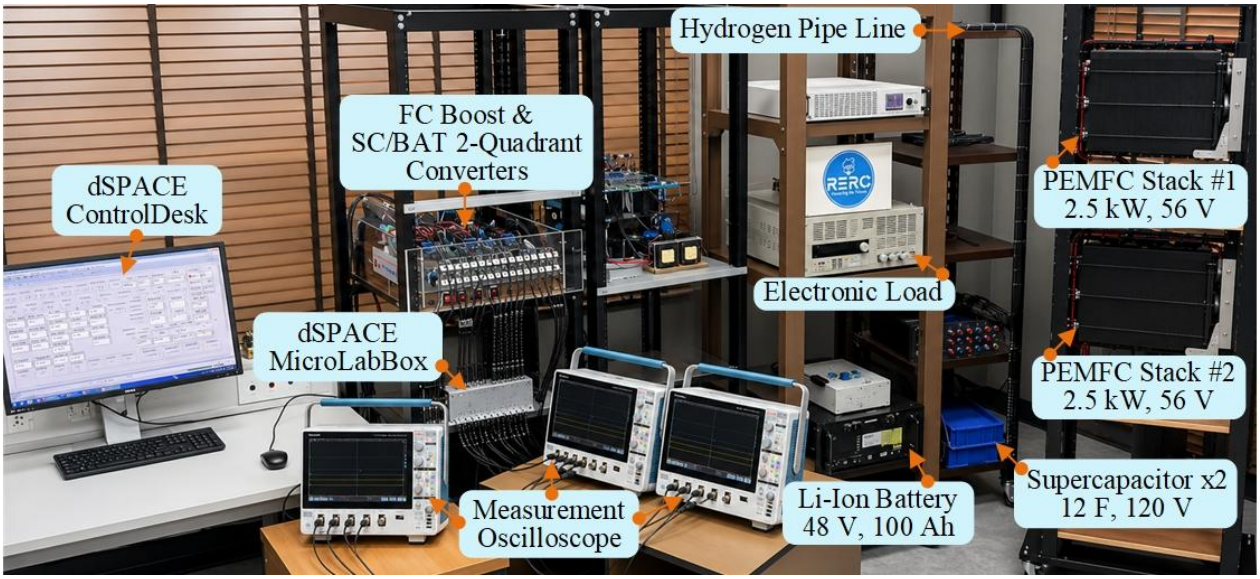


Figure 9. Experimental FC/SC/battery hybrid-source and DC-microgrid platform used for real-time validation. Note # sign means number of stack.

Table 1. Parameters of the hybrid power converters.

Symbol	Parameter	Value/Unit
v_{FC}	Nominal FC input voltage	56 V
v_{SC}	Nominal SC input voltage	120 V
v_B	Nominal battery input voltage	48 V
C_B	Total DC-bus capacitance	500 μF
C_{SC}	Supercapacitance capacitance	12 F
Q_B	Li-Ion battery capacity	100 Ah
$L_1 = L_2 = L_3$	Inductance	96 μH
f_s	Switching frequency	25 kHz
T_s	Sampling period	40 μs

Table 2. Parameters of the proposed hybrid control system.

Parameters of the Hybrid Control	Symbol	Value/Unit
CPC–MFC	ω_s	157.08×10^3 rad/s ($= 2\pi f_s$)
	N_I	5
	K_I	6.82×10^3 s^{-1}
	N_E	15 ($= N_I \times 3$)
	K_{E1}	2.42×10^3 s^{-1}
	ω_{FC}	0.5 rad/s
	ω_B	2 rad/s ($= \omega_{FC} \times 4$)
	ζ_{FC}, ζ_B	1
	K_{E2}	0.2 s^{-1} ($= \omega_B \times 0.1$)
	K_{E3}	0.05 s^{-1} ($= \omega_{FC} \times 0.1$)
AGO	$\eta_{x,I1} = \eta_{x,I2} = \eta_{x,I3}$	3.47×10^4 s^{-1}
	$\eta_{a,I1} = \eta_{a,I2} = \eta_{a,I3}$	6.01×10^8 s^{-2}
	$\eta_{F,I1} = \eta_{F,I2} = \eta_{F,I3} = \eta_{F,E1}$	0.4 s^{-2}
	$\eta_{x,E1}$	3.47×10^3 s^{-1} ($= \eta_{x,I1} \times 0.1$)
	$\eta_{a,E1}$	6.01×10^7 s^{-2} ($= \eta_{a,I1} \times 0.1$)
Power and current limits	$p_{FC,min}$	0 W

$i_{FC,\,min}$, $i_{FC,\,max}$	0 A, 20 A
$i_{B,\,min}$, $i_{B,\,max}$	−25 A, 25 A

4.2. Simulation of Comparative Evaluation of Lumped-Dynamics Observers

The estimation performance of three conventional observers, the ESO, SMO, and HODO, as defined in Appendix B.4 and the proposed AGO was comparatively evaluated through simulation. All observers were tested under identical plant, controller, sampling, and load conditions and the sampling period is T_s= 40 μs, corresponding to f_s= 25 kHz. The observer parameters were selected to provide comparable nominal convergence speeds, and the same parameter values were retained for the experimental tests. The comparison focused on the estimated current-side lumped term $\hat{F}_{I2}$, which represents the fast converter dynamics.

The performance indices defined in Appendix B.5 were selected according to the evaluation conditions. Under noise-free conditions, the normalized integral of time-weighted squared error (ITSE), integral of absolute error (IAE), and overshoot were used to evaluate the dynamic tracking performance. Under measurement-noise conditions, the normalized RMSE, error standard deviation (σ_e), and maximum absolute error (MaxAE) were used to evaluate the estimation accuracy and sensitivity to measurement noise. Figure 10 presents the corresponding estimation responses under (a) noise-free conditions and (b) measurement-noise conditions. The performance indices obtained under noise-free and measurement-noise conditions are summarized in Tables 3 and 4, respectively.

Figure 10a presents the dynamic estimation responses under noise-free conditions. Although all four observers successfully estimate the variation in F_{I2}, they exhibit different convergence speeds, transient errors, and levels of response smoothness. ESO provides the fastest transient response and achieves the lowest accumulated-error indices. The SMO also responds rapidly but exhibits a stepwise response caused by its discontinuous correction mechanism. HODO produces a noticeable overshoot before converging to the actual lumped dynamics. In comparison, the proposed AGO converges more gradually but provides a smooth transient response with low overshoot.

The observer parameters were selected to provide comparable nominal convergence speeds. The comparative evaluation was conducted entirely through simulation, allowing the four observers to be assessed under identical plant, controller, sampling, and load conditions, together with prescribed measurement-noise scenarios. In contrast, the experimental investigation employed only the proposed AGO within the CPC-based MFC framework.

Figure 10b evaluates the sensitivity of the observers to measurement noise. In Figure 10b, different measurement-noise levels were applied, and all four observers received identical noise-corrupted measurement signals at each noise level to ensure a consistent comparison. The introduced noise produces fluctuations in all the estimated signals, with the ESO exhibiting the largest variations. SMO is also affected by high-frequency noise, whereas the HODO provides a smoother estimate. The proposed AGO produces the smallest fluctuations and maintains the closest agreement with the actual lumped dynamics. These results demonstrate that the AGO provides an effective balance between dynamic-estimation performance and measurement-noise attenuation.

For a consistent comparison, all four observers were implemented using the same switching-model simulation, operating conditions, and sampling frequency of 25 kHz (Ts = 40 μs). The observer algorithms were evaluated within the same discrete-time framework, with their calculations designed to be completed within the assigned sampling interval. Although additional phase-lag or estimation-delay metrics could provide complementary information, the selected time-domain performance indices are appropriate for

evaluating the transient estimation accuracy and measurement-noise attenuation of the observers under the investigated conditions.

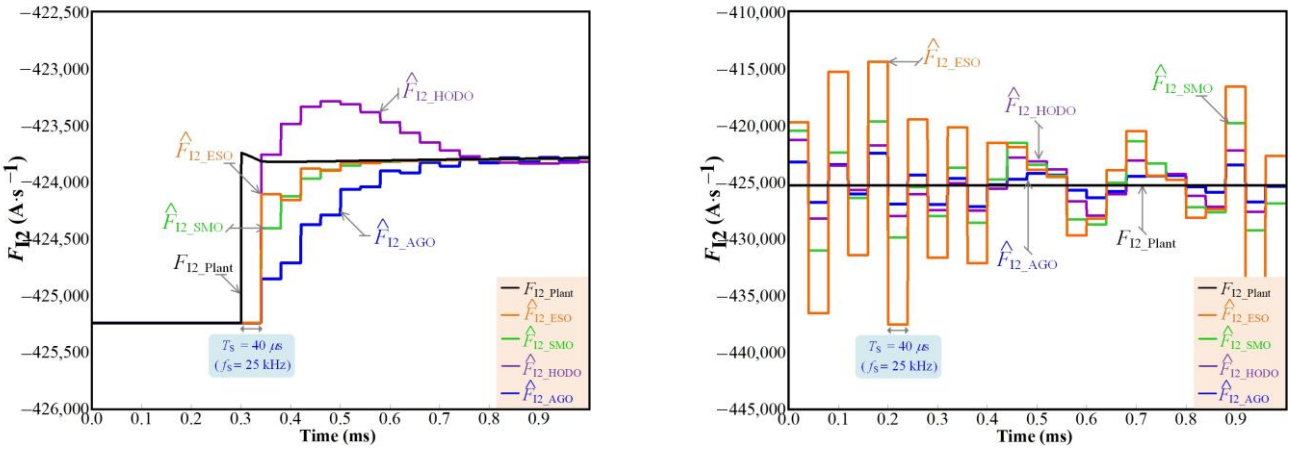


Figure 10. Simulated comparison of the ESO, SMO, HODO, and proposed AGO for estimating the current-side lumped dynamics, $\hat{F}_{I2}$ under a CRL of 30 Ω; (**a**) dynamic estimation performance under noise-free conditions; and (**b**) observer sensitivity to measurement noise.

Table 3. Normalized ITSE, IAE, and overshoot values under noise-free conditions.

Observer	Normalized ITSE (%)	Normalized IAE (%)	Overshoot (%)
ESO	100	100	0
SMO	112	117	0
HODO	173	207	36
Proposed AGO	170	197	0

The ESO value is used as the normalization baseline and is set to 100%.

The quantitative results under noise-free conditions are summarized in Table 3, with the ESO used as the normalization baseline and set to 100% for each index. ESO achieves the lowest normalized ITSE and IAE values. The SMO shows moderate increases in these indices, reaching 112% and 117%, respectively. The proposed AGO yields normalized ITSE and IAE values of 170% and 197%, respectively, which are slightly lower than the corresponding HODO values of 173% and 207%. Moreover, the overshoot of the proposed AGO is 0%, equal to those of the ESO and SMO and lower than the HODO value of 36%. Therefore, although the AGO does not achieve the lowest accumulated-error indices under noise-free conditions, it maintains a smooth response with low overshoot. As reported in Table 4, the proposed AGO achieves the lowest normalized RMSE, σ_e, and MaxAE values under measurement-noise conditions. These values are 20%, 5%, and 21%, respectively. Compared with the ESO baseline, the AGO reduces the RMSE, σ_e, and MaxAE by 80%, 95%, and 79%, respectively. It also outperforms the SMO and HODO across all three indices. These substantial reductions confirm that the proposed AGO provides the strongest measurement-noise attenuation among the evaluated observers while maintaining accurate and smooth estimation.

Table 4. Normalized RMSE, σ_e, and MaxAE values under measurement-noise conditions.

Observer	Normalized RMSE (%)	Normalized σ_e (%)	Normalized MaxAE (%)
ESO	100	100	100
SMO	44	26	48
HODO	29	11	30

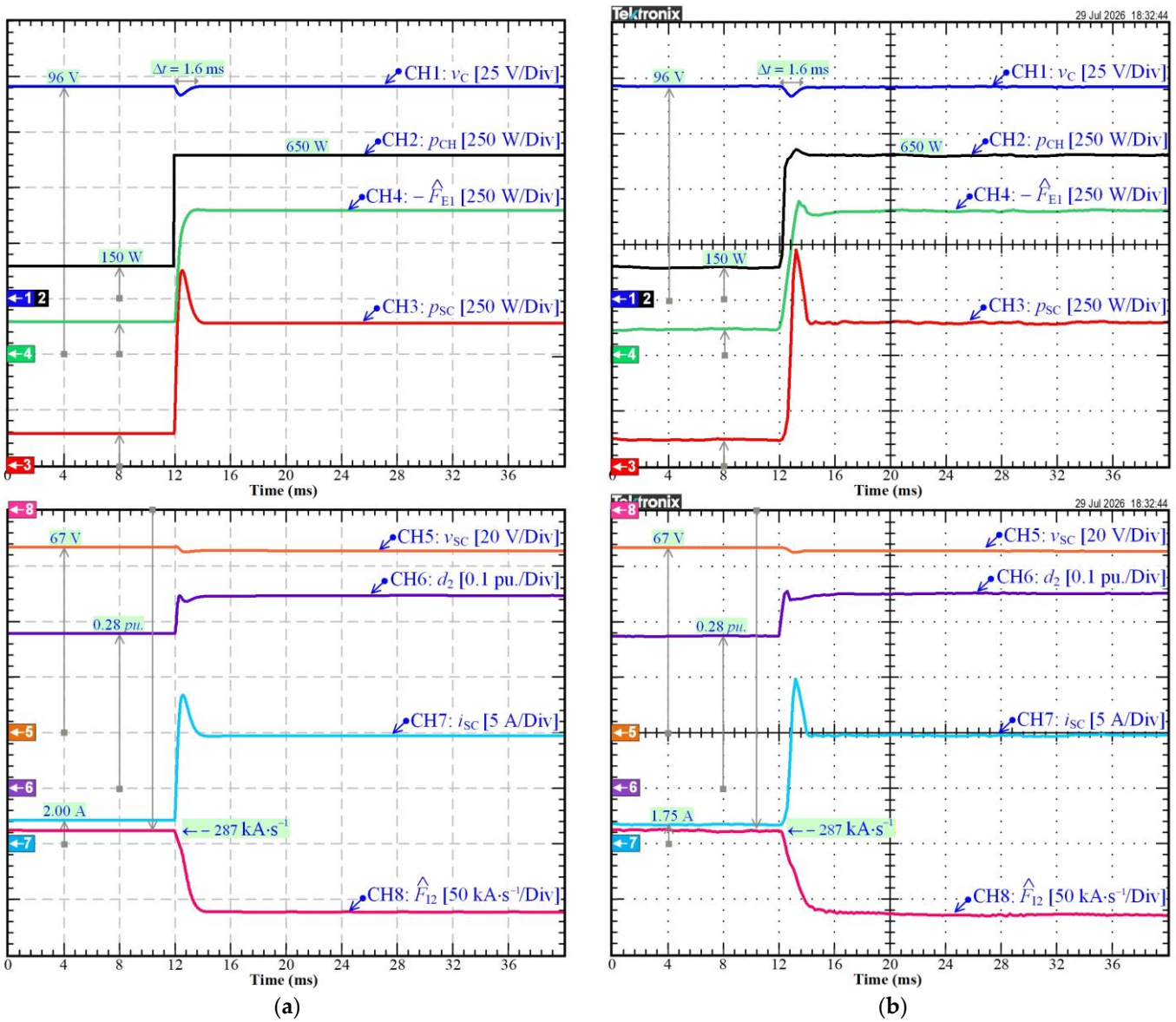
Proposed AGO	20	5	21

The ESO value is used as the normalization baseline and is set to 100%.

The comparative results demonstrate a trade-off between transient estimation speed and measurement-noise attenuation. Although the ESO achieves lower ITSE and IAE values under noise-free conditions, the proposed AGO provides lower RMSE, error standard deviation, and maximum absolute error under the investigated measurement-noise conditions. These results support the noise-attenuation advantage of the AGO under the specified simulation conditions, while the experimental results independently validate the practical feasibility of the complete CPC–AGO-assisted MFC framework.

4.3. Experimental Results

To further evaluate the effectiveness of the proposed control strategy, experimental tests were conducted under three representative operating conditions. First, single-source operation with the FC and battery branches disabled was investigated, as shown in Figure 11. Second, motoring-mode operation was examined in Figure 12. Finally, combined motoring and regenerative-braking operation were evaluated in Figure 13. These tests assess the dynamic performance, robustness, and DC-bus voltage-regulation capability of the proposed method under practical operating conditions.



(**a**) (**b**)

https://doi.org/10.3390/wevj17120631

Figure 11. Single-source dynamic validation with the FC and battery branches disabled under a CPL step from 150 to 650 W: (**a**) simulation results and (**b**) experimental results.

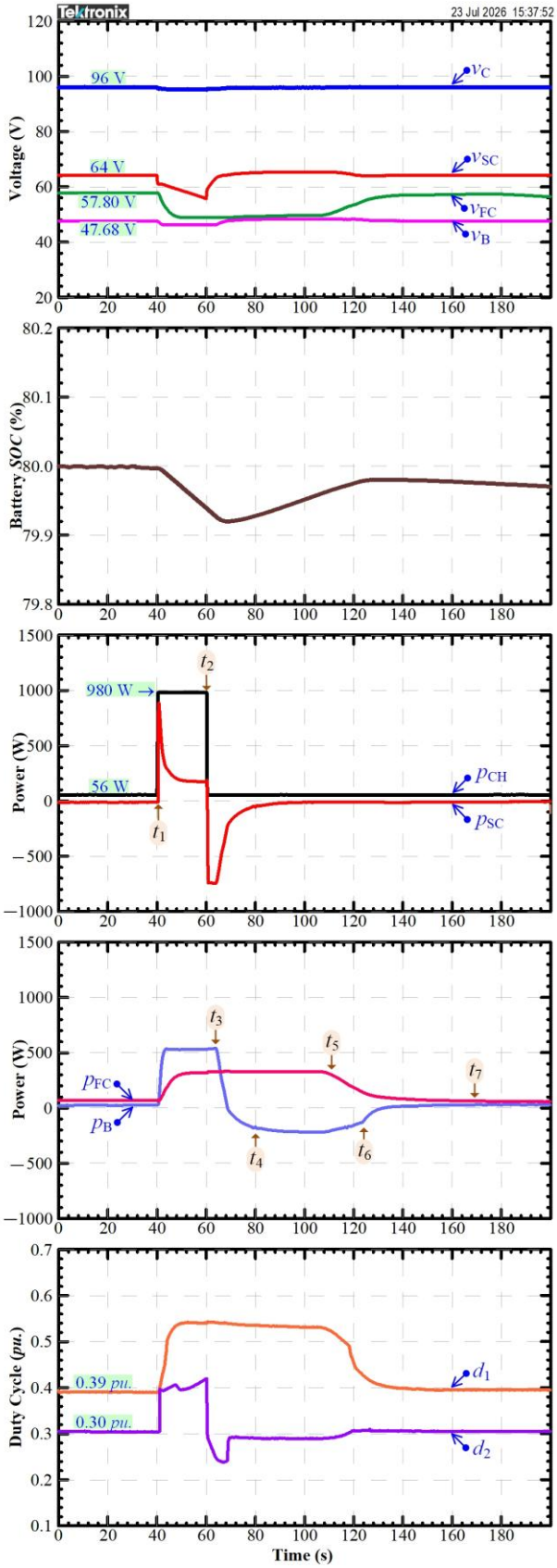
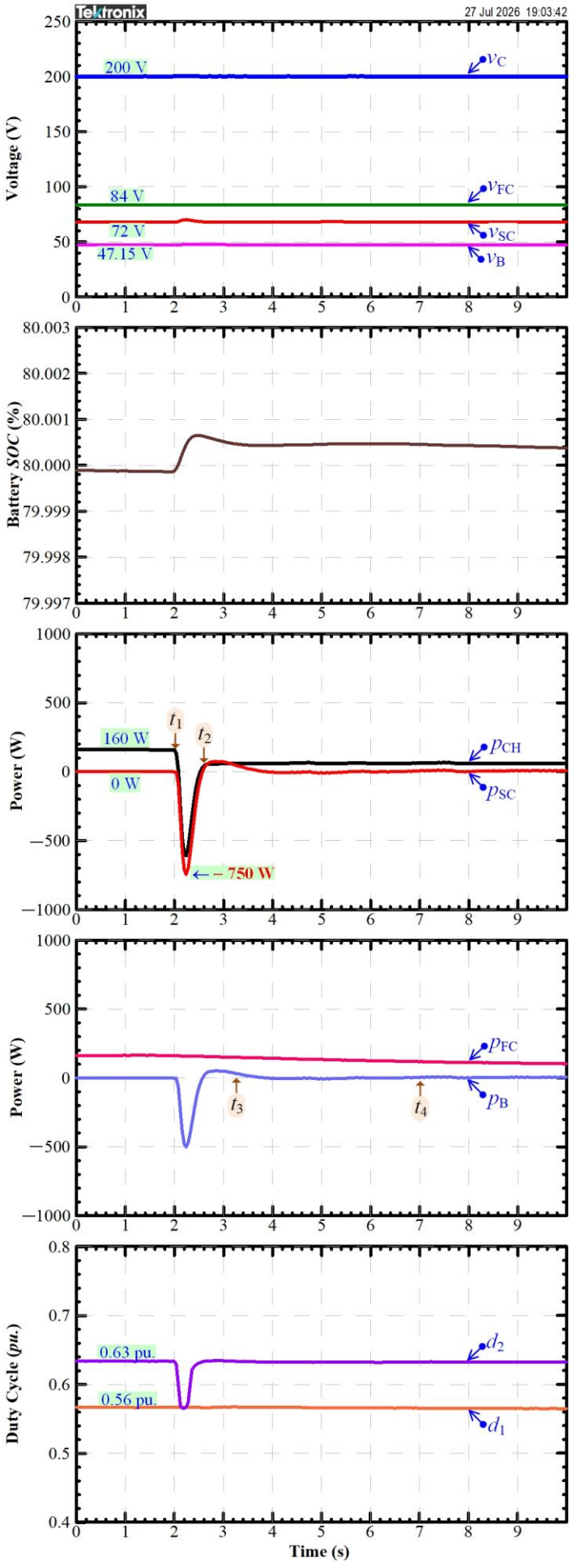


Figure 12. Experimental response of the FC/SC/battery hybrid source to a finite-duration positive load-power in motoring mode.



https://doi.org/10.3390/wevj17120631

Figure 13. Experimental result: response of the FC/SC/battery hybrid source during regenerative braking of the AC traction motor from an initial speed of approximately 420 r/min.

The purpose of the experimental investigation is to validate the real-time feasibility, dynamic response, and energy-management performance of the proposed CPC–AGO framework rather than to compare different observer algorithms experimentally. Comparative evaluations of the AGO, ESO, SMO, and HODO are therefore conducted exclusively through simulation, as presented in Section 4.2. Accordingly, the observer-performance advantages reported in this study are limited to the investigated simulation conditions, while the experimental results demonstrate the practical operation of the proposed framework.

4.3.1. Single-Source Dynamic Validation with FC and Battery Disabled

To evaluate the proposed control strategy under single-source operation, the FC and battery branches were disabled, leaving the SC as the only active power source. Figure 11 compares (a) the simulation results and (b) the experimental results for a CPL step from 150 to 650 W. The same system parameters and controller gains, listed in Tables 1 and 2, respectively, were used in both the simulation and experimental tests. Throughout the test, the SC supplies the entire load-power demand. The nominal SC voltage is 65 V, its initial measured value is approximately 67 V, and the DC-bus voltage reference is set to 96 V. The DC-bus reference of 96 V was selected considering the nominal voltage of the PEMFC stack, approximately 50–56 V, allowing the FC boost converter to operate at a moderate nominal duty ratio near 0.5. This voltage level provides a practical operating point for the laboratory-scale power converter. The oscilloscope channels are defined as follows: CH1, DC-bus voltage v_C [25 V/div]; CH2, load power p_{CH} [250 W/div]; CH3, SC power p_{SC} [250 W/div]; CH4, estimation of the energy-side lumped term $-\hat{F}_{E1}$[250 W/div]; CH5, SC voltage v_{SC} [20 V/div]; CH6, SC-converter duty ratio d_2[0.1 $pu.$/div]; CH7, SC current i_{SC} [5 A/div]; and CH8, estimation of the current-side lumped term $\hat{F}_{I2}$ [50 kA·s^{-1}/div]. As shown in Figure 11a, the simulated DC-bus voltage exhibits only a small transient deviation following the load-power step and returns to its reference value within approximately 1.6 ms. The controller rapidly adjusts the SC-converter duty ratio, causing the SC current and power to increase and meet the higher load demand. The estimated energy- and current-side lumped terms also respond rapidly to the change in operating conditions.

The experimental results in Figure 11b closely agree with the simulation results. Despite the noise measurement and practical converter nonidealities, the DC-bus voltage remains stable and recovers to 96 V within approximately 1.6 ms. The SC power increases to balance the CPL demand, while the duty ratio and SC current exhibit fast and well-damped transient responses. These results confirm the accuracy of the simulation model and demonstrate that the proposed control strategy provides fast and stable DC-bus voltage regulation under CPL operation, even when the FC and battery branches are disabled.

Importantly, Figure 11 provides direct simulation and experimental validation of the integrated CPC–AGO algorithms. In addition to the DC-bus voltage, SC power, and current responses, both results present the SC-converter duty ratio generated by CPC and the online AGO estimates of the energy-side and current-side lumped dynamics, F_E and F_{I2}, respectively. The corresponding transient responses demonstrate the real-time operation of both algorithms within the same closed-loop control system under the investigated CPL disturbance. These results validate the practical feasibility of the proposed CPC–AGO approach without requiring experimental comparisons with alternative observer structures.

It is important to emphasize that neither the load current i_{CH} nor the load-power p_{CH} is used by the AGO or the MFC law. During the experiment, i_{CH} is measured only

for performance evaluation, and the corresponding load power is calculated as $p_{CH} = v_C i_{CH}$. The measured p_{CH} is used exclusively as an independent reference for comparison with $-\hat{F}_{E1}$ in Figure 11. In real-time control, the unknown load-power variation is embedded within $\hat{F}_{E1}$ and reconstructed online by the AGO. Hence, the proposed strategy can therefore regulate the DC bus without a load-current sensor or explicit load-power information, providing a load-power sensorless control capability.

4.3.2. Experimental Result: Motoring-Mode Operation Using a Real 2.5 kW PEMFC System

Figure 12 presents the experimental response of the FC/SC/battery hybrid source to a finite-duration positive load-power pulse in motoring mode using a real 2.5 kW PEMFC stack. During this test, the v_{SC} = 64 V, SOC_d = 80%, and v_{Cd} = 96 V. The FC power limits between $p_{FC,\,min}$ = 0 W, $p_{FC,\,max}$ = 300 W, while the battery power is limited to the range from $p_{B,\,min}$ = -500 W, $p_{B,\,max}$ = 500 W. The corresponding FC and battery current limits are listed in Table 2. The power-management process is divided into seven operating stages, denoted by t_1–t_7. Under the adopted sign convention, positive values of the battery and SC powers indicate that the corresponding source supplies power to the DC bus, whereas negative values indicate power absorption or charging. A programmable electronic load was employed to reproduce controlled CPL disturbances during motoring-mode operation. Unlike the variable power demand of a real traction motor during acceleration, this arrangement enables prescribed constant-power loading conditions to be investigated, which is particularly useful for evaluating DC-bus stability and the transient response of the proposed CPC–AGO framework.

The FC and battery power limits were deliberately selected as 300 W and 500 W, respectively, to validate the source-power-limitation functions of the proposed controller. Although the PEMFC stack is rated at 2.5 kW, the present experiment focuses on control-algorithm validation rather than full-rated-power operation. The load-power step from 56 to 980 W was selected to drive both the FC and battery toward their prescribed power limits, while the SC compensates for the remaining power demand and fast transients. This arrangement enables the experimental evaluation of coordinated power sharing and DC-bus regulation under active source-power constraints.

Before t_1, the system operates under steady-state conditions with a load power of 56 W. The DC-bus voltage is regulated at 96 V, while the initial SC, FC, and battery voltages are 64, 57.80, and 47.68 V, respectively. The battery SOC is approximately 80%, and the initial duty ratios (d_1 and d_2) are 0.39 and 0.30 *pu*, respectively.

At $t_1 \approx 40$ s, the load power is abruptly increased from 56 to approximately 980 W. The SC immediately supplies most of the transient-power demand, thereby preventing a large deviation in the DC-bus voltage. The battery power rapidly increases to approximately 500 W (= $p_{FC,\,max}$) and provides medium-term power support. Meanwhile, the FC power increases more gradually to approximately 300 W because the FC is assigned to supply the slowly varying component of the load demand. During this interval, the SC and FC voltages decrease because of the increased source currents, and the battery SOC decreases from approximately 80% to 79.92%. Nevertheless, the DC-bus voltage remains close to its 96 V reference.

At $t_2 \approx 60$ s, the load power returns to approximately 56 W. When the load power decreases from 980 W to 56 W, the SC changes from discharging to charging and absorbs the transient excess power, as indicated by the negative pulse of p_{SC}. Therefore, the SC rapidly changes from discharging to charging and absorbs the surplus power. The SC power reaches approximately −750 W, preventing an excessive increase in the DC-bus voltage. Both FC and battery are still at their maximum power levels to charge SC and

load-power demand. From approximately 60 to 64 s, the battery power remains nearly constant at about 500 W.

At t_3, subsequently, the battery power gradually decreases and becomes negative, reaching approximately −200 W, indicating that the battery changes from discharging to charging. During this period, the FC continues to supply power, and part of p_{FC} is used to charge the battery.

At t_4, the battery power p_B becomes negative, indicating that the battery is being charged, while p_{SC} gradually returns toward zero. The FC remains at approximately 300 W and supplies both the light load and the power required to recharge the battery. As a result, the SOC gradually recovers toward 80%.

At t_5, as the energy-storage states approach their desired operating levels, the FC power begins to decrease gradually. Accordingly, the magnitude of the battery charging power is reduced around t_6. Meanwhile, the SC power has already returned close to zero, indicating that the SC has completed its transient power-support function.

Finally, during t_7, the FC supplies only the steady load-power demand of at 56 W. The battery power remains close to 0 W because its SOC has recovered close to the 80% reference, while the SC power also remains approximately zero. The duty ratios d_1 and d_2 regulate the converters, and the DC-bus voltage remains stable at approximately 96 V. Overall, the results confirm effective power sharing, energy recovery, and stable DC-bus regulation during motoring operation.

4.3.3. Experimental Result: Regenerative Braking Mode

Figure 13 presents the experimental response of the FC/SC/battery hybrid source during regenerative braking of an AC traction motor from an initial speed of approximately 420 r/min. An FC emulator is used to reproduce the electrical behavior of the FC source while enabling safe high-current operation. Unlike the previous experiments in Figures 11 and 12, where the DC-bus voltage reference was set to 96 V, the reference was increased to 200 V in the regenerative-braking experiment to satisfy the operating requirements of the AC traction drive. This experimental configuration also provides an opportunity to evaluate the proposed CPC–AGO framework at different DC-bus operating points. For regenerative-braking validation, the DC-bus voltage reference was increased to 200 V to satisfy the operating requirements of the AC traction drive.

For the regenerative-braking experiment, the real PEMFC stack was replaced by a conventional DC power supply with a nominal output voltage of approximately 84 V. The power supply serves as an electrical substitute for the FC source rather than reproducing its detailed electrochemical and transient voltage–current characteristics. The objective of this experiment is to validate the proposed CPC–AGO framework during regenerative braking of a real AC traction motor, including SC and battery energy absorption, DC-bus voltage regulation, and prevention of reverse power flow into the FC branch. Therefore, the experimental results demonstrate the feasibility of the proposed regenerative-braking control functions under the investigated conditions, while detailed PEMFC dynamic emulation is outside the scope of the present study.

The proposed CPC–AGO algorithms were implemented using the same controller and observer tuning parameters as in the lower-voltage tests. These experiments demonstrate the practical operation of the proposed framework under different voltage conditions without additional controller-gain retuning. The nominal FC and SC voltages are 84 and 72 V ($= v_{SCd}$), respectively. The FC power's limits are between $p_{FC,\,min} = 0$ W, $p_{FC,\,max} = 400$ W, while the battery power is limited to the range of $p_{B,\,min} = -700$ W to $p_{B,\,max} = 700$ W. The corresponding FC and battery current limits are listed in Table 2. The response is divided into five operating intervals separated by t_1–t_4. Positive source power

represents power delivered to the DC bus, whereas negative battery or SC power indicates regenerative-energy absorption.

At t_1, regenerative braking is initiated. The recovered braking energy causes the SC power p_{SC} to rapidly become negative, reaching approximately −750 W. This indicates that the SC quickly absorbs the regenerative transient energy and prevents a large disturbance in the DC-bus voltage. At the same time, the battery power p_B also becomes negative, reaching approximately −500 W, indicating that part of the recovered energy is transferred to the battery. Consequently, the battery SOC increases slightly. During this transient, the SC voltage increases slightly, whereas the DC-bus voltage remains tightly regulated around 200 V.

Around t_2, as the braking transient decreases, the magnitude of p_{SC} rapidly reduces and returns toward zero. The battery continues to absorb part of the recovered energy for a short period, while the FC power remains positive and changes gradually because of its slower dynamic response. Around t_3, the battery power returns close to zero as the regenerative-energy absorption is completed. The FC power then gradually decreases toward the level required by the remaining load.

Finally, around t_4, both the SC and battery powers remain close to zero, and the system returns to a steady operating condition. The duty ratio d_2 changes rapidly during the braking transient to regulate the SC converter, whereas d_1 varies only slightly because of the slower FC-power dynamics. Throughout the experiment, the DC-bus voltage remains close to its 200 V reference without sustained oscillations. These results demonstrate that the proposed strategy effectively coordinates the SC and battery to absorb regenerative braking energy while maintaining stable DC-bus voltage regulation.

Overall, the experimental results demonstrate that the proposed control strategy effectively coordinates reverse power flow during regenerative breaking. The SC absorbs the rapid, high-power transient component, the battery stores part of the recovered energy, and the FC branch is protected from reverse power flow. Therefore, stable DC-bus voltage regulation and effective regenerative-energy recovery are achieved during the AC traction motor braking test.

The quantitative experimental validation primarily focuses on the dynamic control objectives of the proposed CPC–AGO framework. These include DC-bus voltage regulation under CPL disturbances, coordinated FC/SC/battery power sharing, battery SOC restoration, and regenerative-power absorption. The experimental results demonstrate a DC-bus recovery time of approximately 1.6 ms during the 150–650 W CPL step, gradual FC power variation during the 56–980 W motoring test, battery SOC recovery toward its 80% reference, and transient regenerative-power absorption by the SC and battery. However, the present investigation does not evaluate overall energy-conversion efficiency, hydrogen consumption, or comparative energy efficiency against alternative energy-management strategies. These objectives are outside the scope of the proposed algorithm development and prototype validation.

4.4. Scalability and Applicability to Higher-Power EV Systems

The proposed CPC and AGO algorithms are formulated using general ultra-local models and are not inherently restricted to the power rating of the laboratory prototype. Consequently, the same mathematical control framework can, in principle, be applied to higher-power FC/SC/battery hybrid systems, such as a 60 kW hydrogen fuel-cell electric vehicle, without changing the fundamental CPC and AGO algorithms. However, practical implementation requires appropriate redesign of the power converters and energy-storage systems, together with adjustment of controller gains, observer parameters, sampling frequency, and source-protection limits.

The conceptual 750 V EV architecture presented in Figure 1 illustrates a potential higher-voltage application, whereas the laboratory prototype operates at lower voltage and power levels. The present simulations and experimental results establish the feasibility of the proposed algorithms under the investigated conditions but do not constitute validation of full-scale vehicle performance. Further studies involving higher-power operating conditions and standardized vehicle driving cycles are required to evaluate the performance and practical applicability of the framework at the vehicle scale.

5. Conclusions

This study developed and experimentally validated an accelerated gradient observer (AGO)-assisted continuous predictive control (CPC)-based model-free control framework for an FC/SC/battery hybrid power source. Three outer energy loops and three inner current loops regulate the DC bus, restore the SC energy and battery state of charge, and establish the required dynamic hierarchy among the sources. Command-shaping and protection functions limit the source powers and currents, prevent reverse FC power flow, and restrict rapid FC-power variations. The AGO directly estimates four lumped-dynamics terms, while two energy-side terms are reconstructed algebraically.

The simulation results met the lumped-dynamics estimation objective. Under noise-free conditions, all four observers tracked the current-side lumped term. Although the ESO produced the lowest ITSE and IAE values, the AGO provided a smooth response with low overshoot. Under measurement noise, the AGO achieved the lowest normalized RMSE, error standard deviation, and MaxAE values, corresponding to reductions of 80%, 95%, and 79%, respectively, relative to the ESO.

The experimental results met the energy-management objectives. During the SC-only CPL step from 150 to 650 W, the 96 V DC bus recovered within approximately 1.6 ms. During the 56–980 W motoring test with a real 2.5 kW PEMFC, the SC supplied the immediate transient power, the battery provided intermediate support, and the FC power changed gradually. After the load pulse, the SC energy and battery SOC returned close to their reference values. During regenerative braking, the SC and battery absorbed the returned energy, the 200 V DC bus remained regulated, and the FC power remained nonnegative. The source powers also remained within their imposed limits.

The experimental findings demonstrate stable DC-bus regulation, coordinated transient power sharing, battery SOC restoration, and regenerative-power absorption under the investigated operating conditions. In addition, the FC power-shaping and protection functions restrict abrupt changes in the FC power command. Although limiting rapid FC power variations is expected to mitigate electrochemical stress and contribute to improved PEMFC durability, these potential long-term benefits were not directly evaluated in the present experiments. Therefore, no quantitative improvement in fuel-cell lifetime or degradation is claimed.

Overall, the simulation and experimental results demonstrate that the proposed CPC–AGO framework achieves the defined control objectives under the investigated operating conditions while reducing dependence on detailed parametric models. Future work will focus on standardized vehicle driving cycles, higher-power operation, extended simulation-based comparisons of observers under different operating and measurement-noise conditions, and robustness analysis considering digital sampling, measurement noise, and actuator saturation.

Author Contributions: Conceptualization, O.L., B.N.-M. and P.T.; methodology, O.L., B.N.-M. and P.T.; software, O.L., P.M. and B.Y.; validation, O.L., P.M. and B.Y.; formal analysis, O.L., A.Y. and W.T.; investigation, O.L., P.M. and B.Y.; resources, P.T.; data curation, O.L.; writing—original draft preparation, O.L.; writing—review and editing, P.M., B.Y., S.P., N.B., A.Y., W.T., B.N.-M. and P.T.;

visualization, O.L., A.Y. and W.T.; supervision, A.Y., W.T. and P.T.; project administration, P.T. and W.T.; funding acquisition, P.T. All authors have read and agreed to the published version of the manuscript.

Funding: The doctoral research of O. Lueyos was supported by Rajamangala University of Technology Lanna, Thailand, through the Kaew Kham Lanna Doctoral Scholarship (Grant No. KYKL-66-DENEE-005). This research also received support from King Mongkut's University of Technology North Bangkok, Thailand (Contract No. KMUTNB-70-KNOW-10).

Data Availability Statement: The data presented in this study is available on reasonable requests from the corresponding authors.

Acknowledgments: The authors acknowledge the international research collaboration between King Mongkut's University of Technology North Bangkok, Thailand, and Université de Lorraine, France, within the International Research Partnership "Electrical Engineering–Thai French Research Center (EE-TFRC)", associated with the French PIA project Lorraine Université d'Excellence (LUE), Ref. ANR-15-IDEX-04-LUE. The authors also acknowledge the scientific cooperation with the National University of Science and Technology POLITEHNICA Bucharest, Pitești University Centre, Romania, including collaborative activities associated with the "Nucleu" Program (Project No. 20N/05.01.2023, Component Project PN 23 15 01 02).

Conflicts of Interest: The authors declare no conflicts of interest.

Appendix A. Derivation and Stability Analysis of the CPC-Based MFC Framework

Appendix A.1. Finite-Horizon Derivation of the CPC Law

Substituting the AGO-assisted MFC law in (12) into the ultra-local model in (9) is done. Therefore, the general compensated system is

$$\dot{x}(t) = \lambda(t). \tag{A1}$$

Applying a forward-Euler discretization gives

$$x(k+1) = x(k) + T_s\lambda(k). \tag{A2}$$

In the tracking error in (11), the reference is assumed to remain constant or change negligibly over the short prediction interval. The command $\lambda(k)$ is also assumed to remain constant over the N predicted sampling intervals. Therefore,

$$e(k+j|k) = e(k) + jT_s\lambda(k), \quad j = 1,\ldots,N. \tag{A3}$$

The cumulative finite-horizon tracking cost is defined as

$$J_N(\lambda) = \frac{1}{2}\sum_{j=1}^{N}[e(k) + jT_s\lambda(k)]^2. \tag{A4}$$

The optimal continuous-valued command is obtained from the stationary condition

$$\frac{\partial J_N}{\partial \lambda} = \sum_{j=1}^{N}[e(k) + jT_s\lambda(k)]\,jT_s = 0. \tag{A5}$$

Solving (A5) for $\lambda(k)$ gives

$$\lambda_{CPC}(k) = -\frac{3}{(2N+1)T_s}e(k). \tag{A6}$$

The CPC gain is defined as

$$K_{\mathrm{CPC}}=\frac{3}{(2N+1)T_{\mathrm{s}}}. \tag{A7}$$

Therefore, the closed-form CPC law is

$$\lambda_{\mathrm{CPC}}(k)=-K_{\mathrm{CPC}}e(k). \tag{A8}$$

A smaller prediction horizon N produces a larger CPC gain and a faster desired response. Conversely, a larger prediction horizon produces a smaller gain and smoother desired dynamics. Thus, the prediction horizon provides a direct tuning parameter, while the corresponding feedback gain is determined analytically. The proposed CPC retains the finite-horizon predictive principle but changes the optimized variable. Instead of searching among a finite set of physical control inputs, the CPC analytically determines the continuous-valued command $\lambda_{\mathrm{CPC}}(k)$. This command is then converted into physical control input through the AGO-assisted MFC law.

Appendix A.2. Stability Analysis of the CPC-Based MFC Framework

Consider the tracking error defined in (11). For a constant reference, its derivative is

$$\dot{e}(t)=\lambda_{\mathrm{CPC}}(t). \tag{A9}$$

Substituting the CPC law in (A8) into (A9) gives the nominal closed-loop error dynamics:

$$\dot{e}(t)=-K_{\mathrm{CPC}}e(t). \tag{A10}$$

Consider the following Lyapunov function candidate [36,37]:

$$V(e)=\frac{1}{2}e^2(t) \tag{A11}$$

The function $V(e)$ satisfies

$$V(0)=0,\ V(e)>0 \text{ for all } e\neq 0 \tag{A12}$$

Therefore, $V(e)$ is positive definite. Taking its time derivative along the closed-loop trajectories gives

$$\dot{V}(e)=e(t)\dot{e}(t). \tag{A13}$$

Substituting (A10) into (A13) yields

$$\dot{V}(e)=-K_{\mathrm{CPC}}e^2(t). \tag{A14}$$

Because

$$K_{\mathrm{CPC}}=\frac{3}{(2N+1)T_{\mathrm{s}}}>0,\ N\geq 1,\ T_{\mathrm{s}}>0,\ \dot{V}(e)<0 \text{ for all } e\neq 0 \tag{A15}$$

Thus, $V(e)$ is positive definite and $\dot{V}(e)$ is negative definite. According to Lyapunov's direct method, the equilibrium point $e=0$ is asymptotically stable. Consequently,

$$\lim_{t\to\infty}e(t)=0. \tag{A16}$$

For the complete CPC-based MFC framework, the same analysis applies to the tracking error of each outer energy- and inner current-control loop. Therefore, all outer energy- and inner current-tracking errors converge asymptotically to zero. This nominal stability result holds when the AGO accurately estimates the lumped dynamics, the references remain constant or change negligibly over their respective prediction intervals, and the power, current, and duty-ratio saturation functions remain inactive. □

Appendix B. Formulation and Stability Analysis of the Observer

Appendix B.1. State-Observer Formulation and Estimation-Error Dynamics

Consider the first-order ultra-local model defined in (9):

$$\dot{x}(t) = F(t) + \alpha u(t), \tag{A17}$$

where $x(t)$ is the measured controlled variable, $u(t)$ is the physical control input, $\alpha \neq 0$ is the input-scaling coefficient, and $F(t)$ represents the unknown lumped dynamics.

The state observer is formulated as follows [38]

$$\dot{\hat{x}}(t) = \hat{F}(t) + \alpha u(t) + e_o(t), \tag{A18}$$

where $\hat{x}(t)$ is the estimated state, $\hat{F}(t)$ is the estimate of the lumped dynamics, and $e_o(t)$ is the observer correction signal. The state-estimation error and lumped-dynamics estimation error are respectively defined as

$$e_x(t) = x(t) - \hat{x}(t),\ e_F(t) = F(t) - \hat{F}(t). \tag{A19}$$

Taking the time derivative of $e_x(t)$ gives

$$\dot{e}_x(t) = \dot{x}(t) - \dot{\hat{x}}(t). \tag{A20}$$

Substituting Equations (A17) and (A18) into (A20) gives

$$\begin{aligned} \dot{e}_x(t) &= F(t) + \alpha u(t) - \left[\hat{F}(t) + \alpha u(t) + e_o(t)\right] \\ &= F(t) - \hat{F}(t) - e_o(t). \end{aligned} \tag{A21}$$

Using the definition of $e_F(t)$ in (A19), the observer estimation-error dynamics are obtained as

$$\dot{e}_x(t) = e_F(t) - e_o(t). \tag{A22}$$

Equation (A22) shows that the state-estimation error is governed by the lumped-dynamics estimation error and the observer correction signal. Therefore, the correction signal $e_o(t)$ must be designed to ensure rapid convergence of $e_x(t)$, while $\hat{F}(t)$ must be updated to reduce $e_F(t)$. The accelerated gradient-descent laws used to determine $e_o(t)$ and reconstruct $\hat{F}(t)$ are derived in Appendix B.2.

Appendix B.2. Accelerated Gradient-Descent Learning Law

Conventional disturbance observers, such as the extended-state observer (ESO), reconstruct unknown dynamics through state-estimation error feedback. Although increasing the observer bandwidth can improve convergence speed, high observer gains may amplify measurement noise and produce transient peaking [18,19]. This trade-off motivates the investigation of alternative estimation mechanisms based on gradient-descent optimization.

As a conceptual starting point, consider a first-order gradient-descent observer (GDO). Using the state-estimation error defined in (A19), the corresponding quadratic cost function is

$$J_{GDO}(t) = \frac{1}{2} e_x^2(t).$$

Applying the negative-gradient principle [39–41] gives the observer correction signal

$$e_{o,GDO}(t) = -\eta_x \frac{\partial J_{GDO}(t)}{\partial \hat{x}(t)} = \eta_x e_x(t),\ \eta_x > 0.$$

Thus, the first-order GDO employs a proportional correction driven by the instantaneous state-estimation error. Although this formulation is simple, its state-correction

dynamics depend directly on the selected gradient gain, resulting in a compromise between convergence speed and noise sensitivity.

To provide an additional degree of freedom in the observer correction dynamics, the proposed accelerated gradient observer (AGO) extends this first-order formulation by introducing an auxiliary integral state. The resulting augmented correction mechanism combines the instantaneous estimation error with its integral contribution, as developed in the following equations.

The proposed AGO uses two gradient-descent processes. The first generates the state-observer correction signal $e_o(t)$, while the second updates the lumped-dynamics estimate $\hat{F}(t)$.

State-Estimation Correction Law:

To accelerate the convergence of the state-estimation error, an auxiliary state is introduced as

$$\dot{a}_x(t) = e_x(t). \tag{A23}$$

The augmented state-estimation error is defined as

$$s_x(t) = e_x(t) + \eta_F a_x(t), \ \eta_F > 0. \tag{A24}$$

The accelerated-gradient cost function is selected as

$$J_A = \frac{1}{2} s_x^2. \tag{A25}$$

Applying the negative-gradient principle gives the observer correction signal:

$$e_o(t) = -\eta_x \frac{\partial J_A(t)}{\partial \hat{x}(t)}, \ \eta_x > 0. \tag{A26}$$

Treating $a_x(t)$ as fixed during each instantaneous gradient update gives

$$\frac{\partial J_A(t)}{\partial \hat{x}(t)} = -s_x(t). \tag{A27}$$

Therefore,

$$e_o(t) = \eta_x s_x(t) = \eta_x e_x(t) + \eta_x \eta_F a_x(t). \tag{A28}$$

Defining $\eta_a = \eta_x \eta_F$, the observer correction law becomes

$$e_o(t) = \eta_x e_x(t) + \eta_a a_x(t). \tag{A29}$$

The proposed AGO is therefore expressed as

$$\dot{\hat{x}}(t) = \hat{F}(t) + \alpha u(t) + \eta_x e_x(t) + \eta_a a_x(t). \tag{A30}$$

For $e_F(t) = 0$, substituting (A29) into the estimation-error dynamics in (A22) gives

$$\dot{e}_x(t) = -\eta_x e_x(t) - \eta_a a_x(t). \tag{A31}$$

Differentiating (A31) and using $\dot{a}_x(t) = e_x(t)$ yields

$$\ddot{e}_x(t) + \eta_x \dot{e}_x(t) + \eta_a e_x(t) = 0. \tag{A32}$$

Comparing (A32) with the standard second-order characteristic equation gives

$$\omega_o = \sqrt{\eta_a}, \ \zeta_o = \frac{\eta_x}{2\sqrt{\eta_a}}, \tag{A33}$$

where ω_o and ζ_o are the observer natural frequency and damping ratio, respectively. Thus, the observer gains can be selected as

$$\eta_a = \omega_o^2,\ \eta_x = 2\zeta_o\omega_o. \tag{A34}$$

Lumped-Dynamics Reconstruction Law:

From the estimation-error dynamics in (A22), the observer correction signal satisfies

$$e_o(t) = e_F(t) - \dot{e}_x(t). \tag{A35}$$

Under a local quasi-steady observer condition, the state-estimation error changes slowly, such that $\dot{e}_x(t) \approx 0$. Therefore, $e_o(t) = e_F(t)$. The normalized observer correction signal is defined as

$$s_F(t) = \frac{e_o(t)}{\omega_o}. \tag{A36}$$

Under a local quasi-steady observer condition, $\dot{e}_x(t) \approx 0$. From (A22), $e_o(t) \approx e_F(t)$, and hence

$$s_F(t) \approx \frac{e_F(t)}{\omega_o} = \frac{F(t) - \hat{F}(t)}{\omega_o}. \tag{A37}$$

The lumped-dynamics estimation cost function is selected as

$$J_F(t) = \frac{1}{2}s_F^2(t). \tag{A38}$$

Applying the negative-gradient principle gives

$$\dot{\hat{F}}(t) = -\eta_F \frac{\partial J_F(t)}{\partial \hat{F}(t)},\ \eta_F > 0. \tag{A39}$$

After absorbing the constant normalization factor into the learning coefficient, the compact reconstruction law becomes

$$\dot{\hat{F}}(t) = \eta_F s_F(t), = \eta_F \frac{e_o(t)}{\omega_o}. \tag{A40}$$

Thus, the proposed AGO reconstructs the unknown lumped dynamics from the observer correction signal without requiring an explicit model of $F(t)$. The selection of η_x, η_a, η_F, and ω_o is discussed separately in Appendix C.

Appendix B.3. Stability Analysis of the Proposed AGO

Consider the proposed AGO

$$\dot{\hat{x}} = \hat{F} + \alpha u + e_o,\ \dot{e}_o = -\eta_x e_o + \eta_a e_x,\ \dot{\hat{F}} = \eta_F \frac{e_o}{\sqrt{\eta_a}}, \tag{A41}$$

where $e_x = x - \hat{x}$ and $\eta_x > 0$, $\eta_a > 0$, $\eta_F > 0$. If the lumped dynamics vary negligibly over the observer-convergence interval, such that $\dot{F} = 0$, the state-estimation error e_x, correction signal e_o, and lumped-dynamics estimation error e_F converge asymptotically to zero if $0 < \eta_F < \eta_x\sqrt{\eta_a}$.

Proof. Define the lumped-dynamics estimation error as

$$e_F = F - \hat{F}, \tag{A42}$$

and introduce the following parameters:

$$\omega_o = \sqrt{\eta_a},\ \zeta_o = \frac{\eta_x}{2\sqrt{\eta_a}},\ \lambda_F = \frac{\eta_F}{\eta_a}, \tag{A43}$$

The normalized correction signal and lumped-dynamics estimation error are defined as

$$\bar{e}_o = \frac{e_o}{\omega_o}, \bar{e}_F = \frac{e_F}{\omega_o}. \tag{A44}$$

Using (A41), (A42), and $\dot{F} = 0$, the normalized AGO error dynamics become

$$\dot{e}_x = \omega_o(\bar{e}_F - \bar{e}_o), \tag{A45}$$

$$\dot{\bar{e}}_o = \omega_o e_x - 2\zeta_o \omega_o \bar{e}_o, \tag{A46}$$

$$\dot{\bar{e}}_F = -\lambda_F \omega_o \bar{e}_o. \tag{A47}$$

Consider the following Lyapunov function candidate:

$$V = \frac{1}{2} e_x^2 + \frac{1}{2}\bar{e}_o^2 - \bar{e}_o\bar{e}_F + \frac{\zeta_o}{\lambda_F}\bar{e}_F^2. \tag{A48}$$

The function V is positive definite when $0 < \lambda_F < 2\zeta_o$. Differentiating (A48) along the error dynamics in (A45)–(A47) gives

$$\dot{V} = -\omega_o\left(2\zeta_o - \lambda_F\right)\bar{e}_o^2 \le 0. \tag{A49}$$

Therefore, $\dot{V} = 0$ implies $\bar{e}_o = 0$. From (A45), invariance of this condition requires $e_x = 0$. Subsequently, (A46) requires $\bar{e}_F = 0$. Hence, the largest invariant set contained in $\{\dot{V} = 0\}$ is the origin.

According to LaSalle's invariance principle,

$$e_x(t) \to 0,\ e_o(t) \to 0,\ e_F(t) \to 0 \text{ as } t \to \infty. \tag{A50}$$

Finally, substituting the definitions in (A44) into condition $0 < \lambda_F < 2\zeta_o$ gives

$$\frac{\eta_F}{\eta_a} < \frac{\eta_x}{\sqrt{\eta_a}}, \tag{A51}$$

or equivalently,

$$0 < \eta_F < \eta_x\sqrt{\eta_a}. \tag{A52}$$

Therefore, the proposed AGO is asymptotically stable under the stated condition. □

The nominal stability analysis assumes that the lumped dynamics F vary negligibly during the observer convergence interval. In practical applications, F may change rapidly during load transients, particularly under constant-power-load (CPL) disturbances. Although the proposed AGO continuously updates the lumped-dynamics estimate, rapid variations in F may cause temporary estimation errors because of the finite observer bandwidth. Therefore, the nominal asymptotic stability result is valid under the stated assumptions and does not guarantee exact estimation under arbitrarily fast disturbances.

Appendix B.4. Baseline Observer Used for Comparison

For comparison with the proposed AGO, three conventional observers are considered: the extended-state observer (ESO), sliding-mode observer (SMO), and high-order disturbance observer (HODO). These observers are designed to provide comparable nominal convergence speeds.

Extended State Observer:

Define the state-estimation error as

$$e_x = x - \hat{x}. \tag{A53}$$

The ESO [18] is given by

$$\dot{\hat{x}} = \hat{F} + \alpha u + \beta_1 e_x. \tag{A54}$$

and

$$\dot{\hat{F}} = \beta_2 e_x. \tag{A55}$$

The observer gains are selected as

$$\beta_1 = 2\zeta_o \omega_o, \quad \beta_2 = \omega_o^2, \tag{A56}$$

where $\beta_1 > 0$ and $\beta_2 > 0$ are the observer gains. The ESO provides a conventional second-order benchmark for estimating the unknown lumped dynamics.

Sliding-Mode Observer:

The SMO is expressed as [20]

$$\dot{\hat{x}} = \hat{F} + \alpha u + k_1 \sigma(e_x). \tag{A57}$$

and

$$\dot{\hat{F}} = k_2 \sigma(e_x). \tag{A58}$$

where $k_1 > 0$ and $k_2 > 0$ are the observer gains. The sliding-mode correction can be implemented using the saturation function

$$\sigma(e_x) = \phi \text{sat}\left(\frac{e_x}{\phi}\right), \tag{A59}$$

or, for a smooth boundary-layer implementation, hyperbolic-tangent function

$$\sigma(e_x) = X_b \tanh\left(\frac{e_x}{X_b}\right). \tag{A60}$$

where $\phi > 0$ or $X_b > 0$ determines the boundary-layer width. The observer gains are selected as

$$k_1 = 2\zeta_o \omega_o, \quad k_2 = \omega_o^2. \tag{A61}$$

Thus, the SMO provides a robust bounded-error correction while avoiding an unbounded discontinuous switching term.

High-Order Disturbance Observer:

The second-order HODO directly estimates the lumped dynamics and their first derivative without reconstructing the state x. It is formulated as [21]

$$\hat{F} = \xi_1 + l_1 x, \tag{A62}$$

and

$$\dot{\hat{F}} = \xi_2 + l_2 x, \tag{A63}$$

where ξ_1 and ξ_2 are auxiliary observer states. Their dynamics are given by

$$\dot{\xi}_1 = -l_1(\alpha u + \hat{F}) + \dot{\hat{F}}, \tag{A64}$$

and

$$\dot{\xi}_2 = -l_2(\alpha u + \hat{F}). \tag{A65}$$

The HODO gains are selected as

$$l_1 = 2\zeta_o \omega_o, \quad l_2 = \omega_o^2. \tag{A66}$$

Unlike the ESO and SMO, the HODO does not reconstruct $\hat{x}$; instead, the auxiliary states provide direct estimates of F and $\dot{F}$. This gives a structurally different benchmark for evaluating lumped-dynamics estimation.

Appendix B.5. Observer Performance Indices

The performance of the observers evaluated in Section 4.2, is quantified using the estimation error of the current-side lumped dynamics F_{I2}, defined as

$$e_m = F_{I2} - \hat{F}_{I2,\,m},\ m \in \{ESO, SMO, HODO, AGO\} \tag{A67}$$

where F_{I2} is the actual lumped dynamics ($F_{I2,\,Plant}$) and $\hat{F}_{I2,\,m}$ is the estimate obtained using observer m, and T_f is the total evaluation time. Different indices are used to evaluate the observers under noise-free and measurement-noise conditions.

Noise-Free Conditions:

Under noise-free conditions, the dynamic estimation performance is evaluated using the ITSE, IAE, and overshoot.

The ITSE is defined as [42]

$$ITSE_m = \int_0^{T_f} t\ e_m^2 dt. \tag{A68}$$

This index assigns a larger penalty to estimation errors that persist for a longer time. Therefore, a smaller ITSE indicates faster convergence and a shorter estimation settling time.

The IAE is defined as [43,44]

$$IAE_m = \int_0^{T_f} |e_m(t)|\ dt. \tag{A69}$$

The IAE represents the total magnitude of the estimation error over the evaluation interval.

For a step change in F_{I2} occurring at $t = t_s$, the observer response is normalized as

$$r_m = \frac{\hat{F}_{I2,m} - F_{I2,0}}{F_{I2,ss} - F_{I2,0}}. \tag{A70}$$

where $F_{I2,\,0}$ and $F_{I2,\,ss}$ are the initial and final steady-state values, respectively. The percentage overshoot is calculated as

$$Overshoot_m = \max\left\{0,\ \max_{t_s \le t \le T_f}[r_m - 1]\right\} \times 100\%. \tag{A71}$$

The overshoot index measures the maximum excursion of the estimated response beyond its final steady-state value.

Measurement-Noise Conditions:

Under measurement-noise conditions, the estimation accuracy and noise sensitivity are evaluated using the RMSE, error standard deviation σ_e, and MaxAE.

The RMSE is defined as [42]

$$RMSE_m = \sqrt{\frac{1}{T_f}\int_0^{T_f} e_m^2\, dt}. \tag{A72}$$

The mean estimation error over the selected evaluation interval is

$$\bar{e}_m = \frac{1}{T_f}\int_0^{T_f} e_m\, dt. \tag{A73}$$

The error standard deviation is then defined as

$$\sigma_{e,m}=\sqrt{\frac{1}{T_f}\int_0^{T_f}[e_m - \bar{e}_m]^2\,dt}. \tag{A74}$$

A smaller value of $\sigma_{e,m}$ indicates lower sensitivity to measurement noise and switching ripple.

The maximum absolute error is defined as

$$\mathrm{MaxAE}_m = \max_{0\le t\le T_f}|e_m|. \tag{A75}$$

The MaxAE represents the largest instantaneous absolute estimation error over the evaluation interval. Each performance index is normalized by the corresponding ESO value, which is set to 100%, to enable direct comparison among the observers.

Appendix C. Practical Tuning and Time-Scale Separation

Appendix C.1. CPC Prediction-Horizon Selection

For all CPC loops, the controller gain, as given by (A7) in Appendix A.1, is determined by the prediction horizon N and sampling period T_s. Under ideal compensation of the lumped dynamics, the corresponding closed-loop tracking-error dynamics are approximately first order. Therefore, the equivalent closed-loop bandwidth can be expressed as

$$\omega_{CPC} = K_{CPC}. \tag{A76}$$

Conversely, the prediction horizon corresponding to a desired gain can be obtained from

$$N = \frac{1}{2}\left(\frac{3}{K_{CPC}T_s} - 1\right) \tag{A77}$$

Because N must be a positive integer, the calculated value is rounded to the nearest suitable integer and subsequently verified through simulation or experimental testing. For the experimental system, the switching frequency f_s is given in Table 1. The corresponding sampling period and switching angular frequency are

$$T_s = \frac{1}{f_s},\ \omega_s = 2\pi f_s. \tag{A78}$$

The three inner current-control loops use the same prediction horizon. By selecting $N_I = 5$, their common CPC gain is obtained as

$$K_{I1} = K_{I2} = K_{I3} = K_I = \frac{3}{(2N_I + 1)T_s}. \tag{A79}$$

The DC-bus energy-control loop is designed to respond more slowly than the inner current-control loops. Therefore, its prediction horizon is selected as $N_{E1} = 3N_I = 15$, and the resulting gain is

$$K_{E1} = \frac{3}{(2N_{E1}+1)T_s}. \tag{A80}$$

Consequently, K_{E1} is smaller than K_I, while both gains remain considerably lower than the switching angular frequency. This selection allows the current-control loops to respond rapidly to the power commands, while the DC-bus energy-control loop generates a sufficiently smooth SC power reference.

Appendix C.2. Tuning of the Source Power Dynamics

The FC power dynamics are selected according to the slow electrochemical response of the FC system. The desired FC bandwidth and damping ratio are given in Table 1.

$$\omega_{FC} = 0.5\ s^{-1}, \quad \zeta_{FC} = 1. \tag{A81}$$

The battery is allowed to respond faster than the FC because it can tolerate more rapid power variations. Its desired bandwidth is selected as five times the FC bandwidth:

$$\omega_B = 4\omega_{FC} = 2\ s^{-1}, \quad \zeta_B = 1. \tag{A82}$$

The battery-energy and FC-energy CPC gains are then selected one decade below their associated power-loop bandwidths. Thus,

$$K_{E2} = 0.1\omega_B = 0.2\ s^{-1}. \tag{A83}$$

$$K_{E3} = 0.1\omega_{FC} = 0.05\ s^{-1}. \tag{A84}$$

According to (A81), the corresponding equivalent prediction horizons are approximately $N_{E2} \approx 3.75\times10^5$, $N_{E3} \approx 1.875\times10^6$. Although these equivalent horizons are large, no long-horizon prediction or iterative optimization is performed online. Only the resulting gains K_{E2} and K_{E3} are stored and used in the closed-form CPC laws.

Based on the selected parameters, the numerical time-scale hierarchy is

$$K_{E3} < K_{E2} < \omega_{FC} < \omega_B \ll K_{E1} < K_I \ll \omega_s. \tag{A85}$$

This hierarchy assigns the fastest energy-balancing action to the SC, the intermediate power response to the battery, and the slow average-power response to the FC. It also prevents the FC- and battery-power-shaping dynamics from interfering with the fast DC-bus voltage regulation.

Appendix C.3. AGO Parameter Selection

The AGO parameters are selected according to the desired observer natural frequency in (A33) and (A34) where ω_o and ζ_o are the observer natural frequency and damping ratio, respectively. The observer damping ratio is selected as $\zeta_o = 0.707$ to provide a critically damped estimation response without significant overshoot. The observer natural frequency is selected to be higher than the corresponding CPC closed-loop bandwidth but sufficiently lower than the switching angular frequency:

$$K_I < \omega_o \ll \omega_s. \tag{A86}$$

where K_I is the CPC gain of the control loop and ω_o is its corresponding observer natural frequency. This condition allows the AGO to estimate the lumped dynamics faster than the controller response while limiting the amplification of measurement noise and switching ripple. The lumped-dynamics reconstruction rate is determined by the normalized coefficient

$$\lambda_F = \frac{\eta_F}{\eta_a}. \tag{A87}$$

Based on the stability condition established in Appendix B.3, λ_F must satisfy

$$0 < \lambda_F < 2\zeta_o. \tag{A88}$$

Once λ_F is selected, the lumped-dynamics learning coefficient is calculated as

$$\eta_F = \lambda_F\, \eta_a. \tag{A89}$$

Equivalently, the AGO parameters must satisfy

$$0 < \eta_F < \eta_x \sqrt{\eta_a}. \tag{A90}$$

https://doi.org/10.3390/wevj17120631

In practice, ω_o is initially increased until the estimated lumped dynamics track the actual dynamics with an acceptable convergence speed. If excessive oscillations or noise appear in $\hat{F}$, ω_o or η_F is reduced. The final AGO parameters are selected to provide a compromise between estimation speed, transient overshoot, and noise attenuation while satisfying the stability condition in (A90).

Appendix D. Experimental Test-Bench Specifications and Real-Time Implementation

Appendix D.1. Experimental Equipment and Energy Sources

The experimental platform illustrated in Figures 8 and 9 was developed at the Renewable Energy Research Centre (RERC), King Mongkut's University of Technology North Bangkok, Thailand. It consists of a polymer electrolyte membrane fuel cell (PEMFC), a lithium-ion battery, two supercapacitor (SC) modules, three DC/DC power converters, a programmable electronic load, and measurement instrumentation. The principal equipment specifications, including the manufacturers and model numbers, are summarized in Table A1. The converter electrical parameters and control parameters are provided in Tables 1 and 2, respectively.

The PEMFC system is based on the ME2 Power™ platform, incorporating a 2.5 kW PEMFC stack and a reformer that converts methanol and water into hydrogen. Its nominal system rating is 50 V, whereas the nominal FC input voltage adopted for the present hybrid-converter model is 56 V, as specified in Table 1. The ME2 Power™ PEMFC system incorporates an integrated methanol-to-hydrogen reformer.

Hydrogen is generated from a methanol–water fuel mixture and supplied to the PEMFC stack through the system's internal fuel-processing arrangement. Hydrogen generation and supply are managed by the FC system rather than by the proposed CPC–AGO controller. This configuration has also been documented in our previously published experimental FC studies [13]. Quantitative hydrogen purity, supply pressure, and flow-rate measurements were not independently evaluated in the present study.

The lithium-ion battery is a LEOCH LFeLi-48100TB lithium iron phosphate module with a nominal voltage of 48 V and a capacity of 100 Ah. The SC bank comprises two Maxwell Technologies BMOD0006 E160 C02 modules, each designated as a 160 V/6-F module. According to the manufacturer, the initial rated capacitance is 5.8 F minimum, with a typical value of 6.1 F and a typical equivalent series resistance of 188 mΩ per module. The nominal SC-bank capacitance adopted in the system model is 12 F, as specified

Table A1. Specifications of the experimental test-bench equipment.

Component	Specifications	Manufacturer/Model
PEMFC system	2.5 kW, nominal 50 V; PEMFC with methanol– hydrogen reformer	H2 PowerTech LLC/ME2 Power™
Li-ion battery	$LiFePO_4$, 48 V, 100 Ah	LEOCH/LFeLi-48100TB
Supercapacitors	Two modules, nominal 6 F and 160 V each	Maxwell Technologies/ BMOD0006 E160 C02
DC/DC converters	IGBT: SKM100GB12T4 100 A, 1200 V	RERC/In-house design
Voltage sensors	500 V, linearity error < 0.20%	LEM/LV 25-P
Current sensors	50 A, linearity error < 0.15%	LEM/LA 55-P
Real-time controller	Programmable DC load, 600 V, 840 A, 12 kW	dSPACE/MicroLabBox Version I (DS1202)
Electronic load	Switching frequency	Chroma/63212E-600-840
Oscilloscopes	Four units, four analog channels per unit	Tektronix/MSO44

In Table 1, these three energy sources provide complementary characteristics: the FC supplies the relatively slow-varying power component, the battery provides intermediate energy support, and the SC compensates for rapid power fluctuations and absorbs regenerative energy.

Appendix D.2 Experimental Equipment and Energy Sources

The three DC/DC converters interfacing the FC, SC, and battery with the common DC bus were designed and constructed in-house at RERC. All three converters employ insulated-gate bipolar transistor (IGBT) power switches. Their principal passive-component parameters, including the inductances and DC-link capacitance, are listed in Table 1.

The converters operate at a switching frequency of 25 kHz, synchronized with the real-time control sampling period of 40 μs. Their duty cycles are calculated by the proposed CPC–AGO-assisted model-free control framework.

Appendix D.3. Real-Time Controller and Data Acquisition

The proposed CPC–AGO control framework was implemented using a dSPACE MicroLabBox Version I real-time control platform (DS1202). The platform incorporates a dual-core NXP QorIQ P5020 processor operating at 2 GHz and a Xilinx Kintex-7 XC7K325T FPGA. The hardware also provides high-speed analog inputs, analog outputs, and digital I/O interfaces for measurement acquisition and power-converter control.

The control algorithms were developed using MATLAB/Simulink and implemented on the dSPACE real-time platform. ControlDesk was employed for monitoring the experimental variables, adjusting control parameters, and recording the experimental data. The principal hardware specifications and real-time implementation settings are summarized in Table A2. All voltage measurements were obtained using LEM LV 25-P voltage transducers, while LEM LA 55-P current transducers were employed for current measurements. The measurement signals were supplied to the dSPACE analog input channels for real-time feedback control and observer calculations.

Table A2. Specifications of the dSPACE MicroLabBox real-time control platform.

Parameter	Specifications
Manufacturer	dSPACE GmbH
Real-time control platform	MicroLabBox Version I, DS1202
Real-time CPU	NXP QorIQ P5020, dual-core, 2 GHz
Host communication processor	NXP QorIQ P1011, 800 MHz
RAM	1 GB DRAM
Flash memory	128 MB
FPGA	Xilinx Kintex-7 XC7K325T
High-speed ADC	8 differential channels, 14-bit, 10 MSPS
Standard ADC	24 differential channels, 16-bit, 1 MSPS
Analog input range	±10 V
DAC	16 channels, 16-bit, 1 MSPS
Analog output range	±10 V
Digital I/O	48 bidirectional channels
PWM timing resolution	10 ns
Host communication	Gigabit Ethernet
MATLAB/Simulink	R2018b
dSPACE RTI-MP	Version 7.13
dSPACE ControlDesk	Version 7.1
Control sampling period	40 μs
Control sampling frequency	25 kHz

Converter switching frequency	25 kHz

Four Tektronix MSO44 mixed-signal oscilloscopes, each equipped with four analog input channels, were used for experimental waveform acquisition. The four instruments provide 16 available analog channels in total, allowing multiple source voltages, currents, power responses, and control signals to be observed. The oscilloscopes were employed for waveform monitoring and recording, independently of the real-time control calculations performed by the dSPACE processor. The ADC and DAC conversion rates in Table A2 represent the hardware capabilities of the MicroLabBox. The actual control and observer calculations were executed at the sampling frequency of 25 kHz. The proposed CPC–AGO algorithms were executed on the real-time processor without GPU acceleration.

Appendix D.4. Experimental Operating Conditions and Reproducibility

A Chroma 63212E-600-840 programmable electronic load was used to generate controlled load-power disturbances. The instrument supports constant-current, constant-resistance, constant-voltage, and constant-power operating modes. Its constant-power mode was employed to investigate DC-bus voltage regulation under CPL conditions.

The experimental operating conditions were selected to evaluate the proposed controller under single-source operation, hybrid-source motoring operation, and regenerative braking, as presented in Figures 11–13. In the motoring experiments, the real PEMFC system was used with the FC power limited to 300 W and battery power limited to 500 W to investigate constrained power sharing among the three sources. In the regenerative-braking experiment, the PEMFC was replaced by an external DC power supply with a nominal voltage of approximately 84 V. This arrangement provided the FC-port electrical input for evaluating energy recovery and DC-bus regulation, rather than reproducing the complete electrochemical dynamics of a PEMFC stack.

The nominal equipment ratings, converter parameters, control settings, and operating conditions reported in Tables 1, 2, A1 and A2 provide supplementary information for reproducing the experimental configurations investigated. The results demonstrate the real-time implementation and experimental feasibility of the CPC–AGO-assisted control framework under the specified laboratory conditions.

Historical calibration records and maintenance information for the experimental equipment, together with quantitative state-of-health (SOH) assessments of the PEMFC, battery, and SC modules, were not available for this study. Consequently, the experimental validation focuses on the measured electrical responses and real-time control performance under the specified laboratory operating conditions. Long-term component aging and degradation assessments are outside the scope of the present investigation.

References

1. Pencheva, V.; Asenov, A.; Georgiev, A. Hydrogen Mobility in Bulgaria—Analysis of the Challenges, Prospects and Opportunities for Integration of Transport Systems (Case Study from the City of Ruse). *World Electr. Veh. J.* **2026**, *17*, 100. https://doi.org/10.3390/wevj17020100.
2. Nájera, J.; Arribas, J.R.; Alcalá, E.; Rausell, E.; López Martínez, J.M. Techno-Economic Dimensioning of Hybrid Energy Storage Systems for Heavy-Duty FCHEVs Considering Efficiency and Aging. *World Electr. Veh. J.* **2026**, *17*, 98. https://doi.org/10.3390/wevj17020098.
3. Li, Y.; Wu, Y.; Liu, M.; Xu, L.; Lei, S. Energy Management Strategy for Hydrogen Fuel Cell Tractors Integrating Online Dynamic Response Capability. *World Electr. Veh. J.* **2026**, *17*, 115. https://doi.org/10.3390/wevj17030115.
4. Li, Y.; Lai, B.; Wang, J.; Sun, Y.; Hu, D.; Ding, H. PER-TD3 Integrated with HER Mechanism: Improving Training Efficiency and Control Accuracy for PEMFC Differential Pressure Control. *World Electr. Veh. J.* **2026**, *17*, 195. https://doi.org/10.3390/wevj17040195.

5. Hammer, T.; Mitsching, T.; Heydrich, M.; Ivanov, V. Optimisation and Evaluation of a Fuzzy-Based One-Pedal Driving Strategy for Enhancing Energy Efficiency and Driving Comfort. *World Electr. Veh. J.* **2025**, *16*, 608. https://doi.org/10.3390/wevj16110608.
6. Lin, X.; Tu, J.; Xu, X.; Huang, H.; Zhou, Q. Fuel cell/battery aging-conscious ramp-down power distribution strategy for a hybrid energy storage system-based SOC predicted by using self-learning Markov algorithm. *IEEE Trans. Transp. Electrif.* **2026**, *12*, 1013–1025. https://doi.org/10.1109/TTE.2025.3624384.
7. Yu, P.; Li, M.; Wang, Y.; Chen, Z. Fuel Cell Hybrid Electric Vehicles: A Review of Topologies and Energy Management Strategies. *World Electr. Veh. J.* **2022**, *13*, 172. https://doi.org/10.3390/wevj13090172.
8. Guo, J.; He, H.; Jia, C.; Guo, S. The Energy Management Strategies for Fuel Cell Electric Vehicles: An Overview and Future Directions. *World Electr. Veh. J.* **2025**, *16*, 542. https://doi.org/10.3390/wevj16090542.
9. Mammeri, K.; Bouzidi, R.; Gasbaoui, B.; Ghadbane, H.E.; Benbouhenni, H.; Bizon, N.; Tulbure, A. Adaptive Physics-Informed Digital Twin-Based Energy Management for Dynamic Inductive Charging of Four-Wheel Drive Fuel Cell Hybrid Electric Vehicles. *World Electr. Veh. J.* **2026**, *17*, 458. https://doi.org/10.3390/wevj17090458.
10. Mounica, V.; Obulesu, Y.P. Hybrid Power Management Strategy with Fuel Cell, Battery, and Supercapacitor for Fuel Economy in Hybrid Electric Vehicle Application. *Energies* **2022**, *15*, 4185. https://doi.org/10.3390/en15124185.
11. Steiner, M.; Scholten, J. Energy storage on board of railway vehicles. In Proceedings of the 2005 European Conference on Power Electronics and Applications, Dresden, Germany, 11–14 September 2005; pp. 1–10. https://doi.org/10.1109/EPE.2005.219410.
12. Xu, D.; Liu, Q.; Yan, W.; Yang, W. Adaptive Terminal Sliding Mode Control for Hybrid Energy Storage Systems of Fuel Cell, Battery and Supercapacitor. *IEEE Access* **2019**, *7*, 29295–29303. https://doi.org/10.1109/ACCESS.2019.2897015.
13. Mungporn, P.; Kamnarn, U.; Yodwong, B.; Khomfoi, S.; Pierfederici, S.; Nahid-Mobarakeh, B.; Vitale, G.; Bizon, N.; Thounthong, P. Hamiltonian-Based Approach to Enhance the Stability of Hybrid Fuel Cell and Supercapacitor Sources. *IEEE Open J. Ind. Appl.* **2025**, *6*, 565–578. https://doi.org/10.1109/OJIA.2025.3591144.
14. Khalid, M. Passivity-Based Nonlinear Control Approach for Efficient Energy Management in Fuel Cell Hybrid Electric Vehicles. *IEEE Access* **2024**, *12*, 84169–84188. https://doi.org/10.1109/ACCESS.2024.3412888.
15. Amin; Bambang, R.T.; Rohman, A.S.; Dronkers, C.J.; Ortega, R.; Sasongko, A. Energy Management of Fuel Cell/Battery/Supercapacitor Hybrid Power Sources Using Model Predictive Control. *IEEE Trans. Ind. Inform.* **2014**, *10*, 1992–2002. https://doi.org/10.1109/TII.2014.2333873.
16. Fliess, M.; Join, C. Model-free control. *Int. J. Control* **2013**, *86*, 2228–2252. https://doi.org/10.1080/00207179.2013.810345.
17. Wang, F.; Wei, Y.; Rodriguez, J.; Garcia, C. State-of-Art, Development, and Challenges of Model-Free Predictive Control on Motor Drives. *IEEE Trans. Power Electron.* **2025**, *40*, 10846–10864. https://doi.org/10.1109/TPEL.2025.3559514.
18. Zhang, Y.; Jin, J.; Huang, L. Model-free predictive current control of PMSM drives based on extended state observer using ultralocal model. *IEEE Trans. Ind. Electron.* **2021**, *68*, 993–1003. https://doi.org/10.1109/TIE.2020.2970660.
19. Zhao, G.; Cui, B.; Wang, P.; Xia, Y.; Zhang, Y. A filter-based extended state observer with arbitrary noise suppression ability and its application to drag-free spacecraft system. *IEEE Trans. Autom. Sci. Eng.* **2025**, *22*, 16403–16414. https://doi.org/10.1109/TASE.2025.3574422.
20. Do, T.A.; Pham, Q.H.; Giap, V.N.; Nguyen, Q.D.; Vu, P. Homogeneous disturbance observer based on sliding mode observer and controller for T-type inverter. *J. Electr. Eng. Technol.* **2024**, *19*, 1671–1683. https://doi.org/10.1007/s42835-023-01685-8.
21. Pham, V.-C.; Tran, N.; Ngo, H.-H.; Mac, P.; Tran, H. Robust optimal control for two-wheeled inverted pendulum via hierarchical sliding mode control and high-order disturbance observer with off-policy adaptive dynamic programming. *J. Control Autom. Electr. Syst.* **2026**, *37*, 746–763. https://doi.org/10.1007/s40313-026-01280-y.
22. Wei, Y.; Chen, Y.; Young, H.; Ou, K.; Yuan, K.; Wu, X.; Wang, F.; Huang, S. Online Data-Gradient-Based Optimized Ultralocal Model-Free Predictive Control for PMSM Drives. *IEEE Trans. Transport. Electrific.* **2026**, *12*, 4999–5012. https://doi.org/10.1109/TTE.2026.3665734.
23. Bierlaire, M. *Optimization: Principles and Algorithms*, 2nd ed.; EPFL Press: Lausanne, Switzerland, 2018.
24. Thounthong, P.; Raël, S.; Davat, B. Control strategy of fuel cell and supercapacitors association for a distributed generation system. *IEEE Trans. Ind. Electron.* **2007**, *54*, 3225–3233. https://doi.org/10.1109/TIE.2007.896477.
25. Restrepo, C.; Konjedic, T.; Guarnizo, C.; Aviñó-Salvadó, O.; Calvente, J.; Romero, A.; Giral, R. Simplified mathematical model for calculating the oxygen excess ratio of a PEM fuel cell system in real-time applications. *IEEE Trans. Ind. Electron.* **2014**, *61*, 2816–2825. https://doi.org/10.1109/TIE.2013.2276331.
26. Suh, K.-W.; Stefanopoulou, A.G. Performance limitations of air flow control in power-autonomous fuel cell systems. *IEEE Trans. Control Syst. Technol.* **2007**, *15*, 465–473. https://doi.org/10.1109/TCST.2007.894640.

27. Zhang, X.; Xu, K.; Du, H.; Ma, X.; Qin, Y.; Shuai, S.; Xuan, F. From Channel Flooding to Voltage Instability: Investigating the Impact Mechanism in Proton Exchange Membrane Fuel Cells. *J. Power Sources* **2026**, *670*, 239366. https://doi.org/10.1016/j.jpowsour.**2026**.239366.
28. Menhour, L.; d'Andréa-Novel, B.; Fliess, M.; Gruyer, D.; Mounier, H. An efficient model-free setting for longitudinal and lateral vehicle control: Validation through the interconnected Pro-SiVIC/RTMaps prototyping platform. *IEEE Trans. Intell. Transp. Syst.* **2018**, *19*, 461–475. https://doi.org/10.1109/TITS.2017.2699283.
29. Zhou, Y.; Li, H.; Liu, R.; Mao, J. Continuous voltage vector model-free predictive current control of surface mounted permanent magnet synchronous motor. *IEEE Trans. Energy Convers.* **2019**, *34*, 899–908. https://doi.org/10.1109/TEC.2018.2867218.
30. Zhang, Y.; Jiang, T.; Jiao, J. Model-free predictive current control of DFIG based on an extended state observer under unbalanced and distorted grid. *IEEE Trans. Power Electron.* **2020**, *35*, 8130–8139. https://doi.org/10.1109/TPEL.2020.2967172.
31. Park, B.; Olama, M.M. A model-free voltage control approach to mitigate motor stalling and FIDVR for smart grids. *IEEE Trans. Smart Grid* **2021**, *12*, 67–78. https://doi.org/10.1109/TSG.2020.3012308.
32. Gaeid, K.S.; Nashee, A.F.; Ali, S.H. Artificial Intelligence Hybrid Control Technique of DC/DC Boost Converter for EV Battery and Motor Load Systems. *World Electr. Veh. J.* **2026**, *17*, 552. https://doi.org/10.3390/wevj17110552.
33. Lueyos, O.; Mungporn, P.; Yodwong, B.; Pierfederici, S.; Yodjaiphet, A.; Thipprasert, W.; Nahid-Mobarakeh, B.; Thounthong, P. Energy shaping and damping control based on Hamiltonian control law of hydrogen fuel cell/supercapacitor/battery hybrid source for DC microgrid stability. In Proceedings of the 2026 IEEE IAS Industrial and Commercial Power System Asia (I&CPS Asia 2026), Kunming, China, 11–14 July 2026; pp. 821–826. https://doi.org/10.1109/ICPSAsia70813.2026.11692294.
34. Qin, X.; Tan, Z.; Xu, Q.; Cai, L.; Zou, X.; Dai, N. Enhanced Battery Pack Consistency: A Hierarchical Active Balancing System Combining Bidirectional Buck–Boost and Flyback Converters. *World Electr. Veh. J.* **2026**, *17*, 231. https://doi.org/10.3390/wevj17050231.
35. Habib, H.F.; Hariri, M.E.; Elsayed, A.; Mohammed, O.A. Utilization of supercapacitors in protection schemes for resiliency against communication outages: A case study on size and cost optimization. *IEEE Trans. Ind. Appl.* **2018**, *54*, 3153–3164. https://doi.org/10.1109/TIA.2018.2819620.
36. Anju, M.; Shihabudheen, K.V.; Mija, S.J. Adaptive recurrent neural network-based ADRC supplementary damping controller for SSO mitigation in type-3 wind power systems. *IEEE Trans. Power Deliv.* **2025**, *40*, 2918–2930. https://doi.org/10.1109/TPWRD.2025.3602968.
37. Xu, D.; Yang, Y.; Lam, C.-S.; Huang, S.; Yang, X.; Li, H. Fixed-time/preassigned-time dynamic surface control of power systems with capacitive-coupled STATCOM. *IEEE Trans. Power Deliv.* **2024**, *39*, 1697–1709. https://doi.org/10.1109/TPWRD.2024.3376460.
38. Li, Y.; Hu, Y.; Luo, Z. Position estimation error reduction based on first-order complex-coefficient extended state observer for IPMSM sensorless drives. *IEEE Trans. Ind. Appl.* **2025**, *61*, 3104–3113. https://doi.org/10.1109/TIA.2025.3531829.
39. Xie, Y.; Li, Y.; Gu, Y.; Cao, J.; Chen, B. Fixed-point minimum error entropy with fiducial points. *IEEE Trans. Signal Process.* **2020**, *68*, 3824–3833. https://doi.org/10.1109/TSP.2020.3001404.
40. Santra, S.; Hsieh, J.-W.; Lin, C.-F. Gradient descent effects on differential neural architecture search: A survey. *IEEE Access* **2021**, *9*, 89602–89618. https://doi.org/10.1109/ACCESS.2021.3090918.
41. Gaudio, J.E.; Annaswamy, A.M.; Bolender, M.A.; Lavretsky, E.; Gibson, T.E. A class of high order tuners for adaptive systems. *IEEE Control Syst. Lett.* **2021**, *5*, 391–396. https://doi.org/10.1109/LCSYS.2020.3002513.
42. Sami, I.; Ullah, S.; Ullah, S.; Bukhari, S.S.H.; Ahmed, N.; Salman, M.; Ro, J.-S. A Non-Integer High-Order Sliding Mode Control of Induction Motor with Machine Learning-Based Speed Observer. *Machines* **2023**, *11*, 584. https://doi.org/10.3390/machines11060584.
43. Mayingi, B.A.; Thango, B.A.; Okojie, D.E.; Iqbal, F. Hybrid Particle Whale Optimization for Dual-Output EV Fast-Charging Parameter Estimation. *World Electr. Veh. J.* **2026**, *17*, 440. https://doi.org/10.3390/wevj17090440.
44. Dong, Q.; Liu, Z.; Wang, H.; Wang, L.; Dong, R.; Lv, L. SOH Estimation of Lithium Battery Under Improved CNN-BIGRU-Attention Model Based on Hiking Optimization Algorithm. *World Electr. Veh. J.* **2025**, *16*, 487. https://doi.org/10.3390/wevj16090487.

Disclaimer/Publisher's Note: The statements, opinions and data contained in all publications are solely those of the individual author(s) and contributor(s) and not of MDPI and/or the editor(s). MDPI and/or the editor(s) disclaim responsibility for any injury to people or property resulting from any ideas, methods, instructions or products referred to in the content.